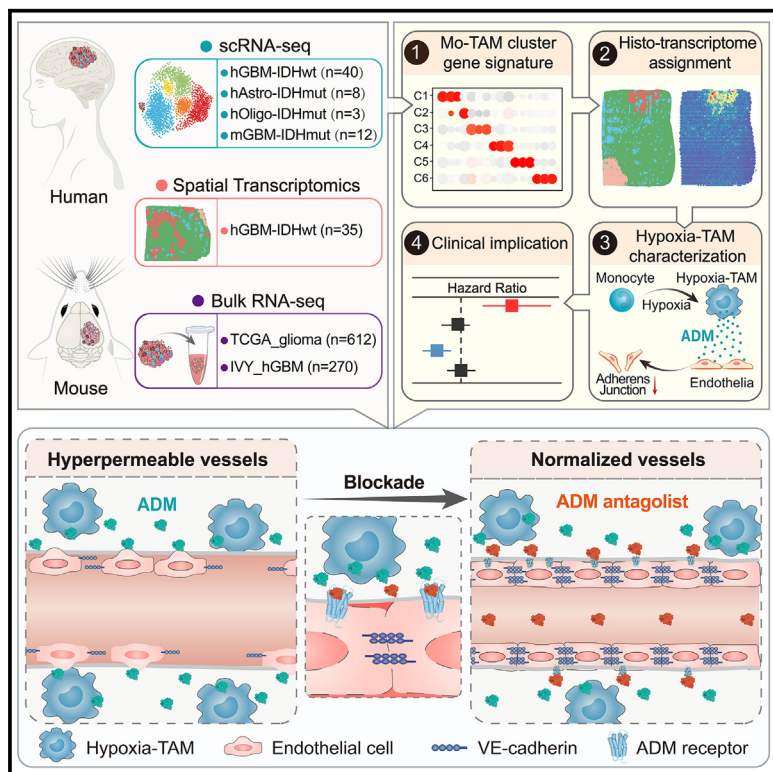


Identification of hypoxic macrophages in glioblastoma with therapeutic potential for vasculature normalization

Graphical abstract



Authors

Wenying Wang, Tianran Li,
Yue Cheng, ..., Yi-Fang Ping,
Xiu-Wu Bian, Yu Shi

Correspondence

pingyifang@126.com (Y.-F.P.),
bianxiuwu@263.net (X.-W.B.),
shiyu@tmmu.edu.cn (Y.S.)

In brief

Pronounced necrosis in glioblastomas is accompanied by abundant destabilized microvessels. Wang et al. show that the niche cues from the peri-necrotic regions polarize macrophages toward a hypoxic state, which in turn augments vascular hyperpermeability. Targeting adrenomedullin produced by hypoxic macrophages normalizes tumor neovasculature and improves anti-tumor drug delivery and efficacy.

Highlights

- Single-cell omics reveals functional and spatial diversity of Mo-TAMs in glioblastomas
- Tumor cues and hypoxia concertedly induce Hypoxia-TAM signature via activating p50
- ADM secreted by Hypoxia-TAM stimulates a destabilized tumor vasculature
- ADM blockade improves vessel integrity, drug delivery, and anti-tumor efficacy



Article

Identification of hypoxic macrophages in glioblastoma with therapeutic potential for vasculature normalization

Wenying Wang,^{1,7} Tianran Li,^{1,7} Yue Cheng,^{1,7} Fei Li,^{2,7} Shuhong Qi,^{3,7} Min Mao,¹ Jingjing Wu,¹ Qing Liu,¹ Xiaoning Zhang,¹ Xuegang Li,² Lu Zhang,¹ Haoyue Qi,¹ Lan Yang,¹ Kaidi Yang,¹ Zhicheng He,¹ Shuaishuai Ding,¹ Zhongyi Qin,^{1,4} Ying Yang,¹ Xi Yang,¹ Chunhua Luo,¹ Ying Guo,¹ Chao Wang,¹ Xindong Liu,¹ Lei Zhou,¹ Yuqi Liu,¹ Weikai Kong,¹ Jingya Miao,¹ Shuanghui Ye,¹ Min Luo,¹ Lele An,¹ Lujing Wang,¹ Linrong Che,⁴ Qin Niu,¹ Qinghua Ma,¹ Xia Zhang,¹ Zhihong Zhang,³ Rong Hu,² Hua Feng,² Yi-Fang Ping,^{1,5,6,*} Xiu-Wu Bian,^{1,5,6,*} and Yu Shi^{1,5,6,8,*}

¹Institute of Pathology and Southwest Cancer Center, Southwest Hospital, Third Military Medical University (Army Medical University), and The Key Laboratory of Tumor Immunopathology, The Ministry of Education of China, Chongqing 400038, P.R. China

²Department of Neurosurgery and Glioma Medical Research Center, Southwest Hospital, Third Military Medical University (Army Medical University), Chongqing 400038, P.R. China

³Britton Chance Center for Biomedical Photonics, Wuhan National Laboratory for Optoelectronics, and MoE Key Laboratory for Biomedical Photonics, School of Engineering Sciences, Huazhong University of Science and Technology, Wuhan 430074, Hubei, P.R. China

⁴Department of Gastroenterology, Chongqing Key Laboratory of Digestive Malignancies, Daping Hospital, Third Military Medical University (Army Medical University), Chongqing 400042, P.R. China

⁵Chongqing Advanced Pathology Research Institute, Jinfeng Laboratory, Chongqing 400039, P. R. China

⁶Yu-Yue Scientific Research Center for Pathology, Jinfeng Laboratory, Chongqing 400039, P.R. China

⁷These authors contributed equally

⁸Lead contact

*Correspondence: pingyifang@126.com (Y.-F.P.), bianxiuwu@263.net (X.-W.B.), shiyu@tmmu.edu.cn (Y.S.)

<https://doi.org/10.1016/j.ccel.2024.03.013>

SUMMARY

Monocyte-derived tumor-associated macrophages (Mo-TAMs) intensively infiltrate diffuse gliomas with remarkable heterogeneity. Using single-cell transcriptomics, we chart a spatially resolved transcriptional landscape of Mo-TAMs across 51 patients with isocitrate dehydrogenase (IDH)-wild-type glioblastomas or IDH-mutant gliomas. We characterize a Mo-TAM subset that is localized to the peri-necrotic niche and skewed by hypoxic niche cues to acquire a hypoxia response signature. Hypoxia-TAM destabilizes endothelial adherens junctions by activating adrenomedullin paracrine signaling, thereby stimulating a hyperpermeable neovasculature that hampers drug delivery in glioblastoma xenografts. Accordingly, genetic ablation or pharmacological blockade of adrenomedullin produced by Hypoxia-TAM restores vascular integrity, improves intratumoral concentration of the anti-tumor agent dabrafenib, and achieves combinatorial therapeutic benefits. Increased proportion of Hypoxia-TAM or adrenomedullin expression is predictive of tumor vessel hyperpermeability and a worse prognosis of glioblastoma. Our findings highlight Mo-TAM diversity and spatial niche-steered Mo-TAM reprogramming in diffuse gliomas and indicate potential therapeutics targeting Hypoxia-TAM to normalize tumor vasculature.

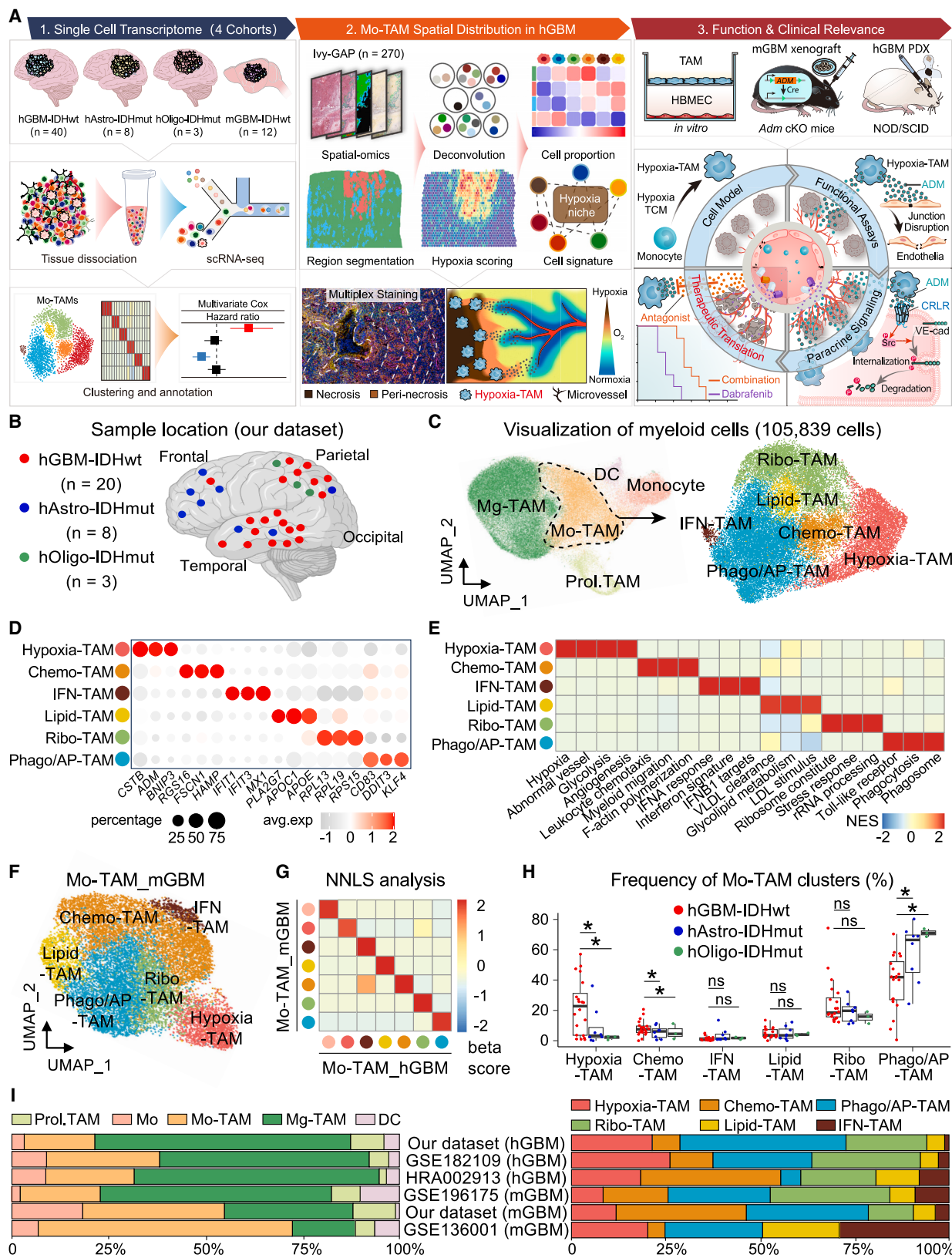
INTRODUCTION

Diffuse gliomas, comprising isocitrate dehydrogenase (IDH)-wild-type (wt) glioblastoma (GBM) and IDH-mutant astrocytoma and oligodendrogloma, are the most prevalent malignant brain tumors in adults.¹ Tumor-associated macrophages (TAMs) are the prevailing immune infiltrates in diffuse gliomas.² TAMs directly interact with malignant cells to fuel tumor progression^{3,4} and act as an architect of the immune-suppressive microenvironment.^{5,6} Therefore, TAMs have emerged as an attractive therapeutic target. Currently, several TAM-targeting approaches are being tested, with the aim of perturbing TAM recruitment or survival,⁷

revitalizing TAM phagocytosis,⁸ reprogramming TAM phenotype,⁹ or transferring gene-edited macrophages.¹⁰ However, no compelling efficacy of these strategies has been observed in large-scale clinical trials,¹¹ which may stem from the remarkable cellular diversity and plasticity of TAM pool within and across tumors.¹² Therefore, dissecting molecular and functional heterogeneity of TAMs with distinct ontogenetic origins is a prerequisite for the rational design of effective TAM-targeting therapy.

TAMs in diffuse gliomas are largely derived from peripheral monocytes (monocyte-derived TAMs [Mo-TAMs]) or brain-resident microglia (microglia-derived TAMs [Mg-TAMs]).^{13,14} Unlike monocyte-derived macrophages resident in normal tissues that





(legend on next page)

exhibit homeostatic and antimicrobial functions, Mo-TAMs infiltrating gliomas are generally tumor supportive and extremely versatile. They differ from Mg-TAMs in the aspects of their distinct gene markers, predominant distribution within the tumor core, and increased cell frequency in GBM-IDHwt and recurrent gliomas.^{13,15} In particular, remarkable transcriptional heterogeneity within Mo-TAMs has been found in multiple tumors.^{16–19} The advent of single-cell RNA sequencing (scRNA-seq) and spatial transcriptomic technologies allow for the interrogation of spatially resolved transcriptional programs and cellular interactions in segregated tumor niches,^{20–22} providing powerful tools for exploring the diversity of tumor-infiltrating immune cells in a spatio-temporal fashion. However, the functionality of diverse Mo-TAM subsets and whether their phenotypes are spatially restricted or steered by specific niche cues remain largely unknown.

In this study, by applying integrated single-cell and spatial transcriptomic analyses of myeloid cells across 51 cases of diffuse gliomas, we charted the Mo-TAM landscape and identified six functionally and spatially discrete clusters. Notably, we identified a Mo-TAM cluster that exhibited a hypoxia response signature (Hypoxia-TAM) and was predominantly localized to the peri-necrotic hypoxic tumor niche. As a hallmark of solid tumors, hypoxia is associated with tumor necrosis, neovascularization, and the generation of various inflammatory and chemotactic factors.²³ Hypoxic tumor cues are spatially restricted and may steer genomic instability, transcriptional adaption, and metabolic reprogramming of tumor and niche cells.²⁴ In addition, enhanced TAM recruitment and immunosuppressive tumor-myeloid cell interactions in the hypoxic niche potentiate glioma resistance to chemo- and immuno-therapeutics.^{25,26} This prompts us to determine how hypoxic niche cues skew the Hypoxia-TAM signature and how Hypoxia-TAM interacts with other cells to fuel tumor progression.

Through integrated computational and functional analyses, we uncovered how hypoxic tumor cues induce Hypoxia-TAM polarization. Moreover, we identified a spatial association between Hypoxia-TAM and destabilized microvessels in the peri-necrotic regions of human GBMs (hGBMs). Further investigation revealed Hypoxia-TAM as a direct contributor to hyperpermeable tumor vasculature and adrenomedullin (ADM) oversecreted by Hypoxia-TAM as an orchestrator for destabilizing endothelial junctions. ADM has been recognized as a vasoactive peptide that regulates various cardiovascular-related pathophysiolgies.²⁷ ADM-targeting antibodies or drugs targeting the ADM receptor calcitonin receptor-like receptor (CRLR) heralds promise in

treating cardiogenic shock and migraine.²⁷ To implement our findings into clinical settings, we evaluated the therapeutic potential of ADM antagonist (AMA) as a vascular normalizing agent to restore endothelial junctions, thereby improving anti-tumor drug delivery. Our findings provide new insights into Mo-TAM diversity across diffuse gliomas and shed light on potential therapies targeting Hypoxia-TAM for normalizing tumor vasculature.

RESULTS

Single-cell transcriptomics of myeloid cells in diffuse gliomas

We obtained scRNA-seq data derived from 51 cases of diffuse gliomas in human and 12 cases of mouse GBM (mGBM) specimens and dissected myeloid cell composition and Mo-TAM cellular diversity (Figure 1A). Tumor specimens were derived from patients diagnosed with GBM-IDHwt ($n = 40$), IDH-mutant astrocytoma (Astro-IDHmut, $n = 8$) and IDH-mutant oligodendrogloma (Oligo-IDHmut, $n = 3$) (Figure 1A, and Table S1). Thirty-one glioma specimens of our dataset were located in different lobes of the cerebrum (Figure 1B). Through unbiased clustering and cell lineage annotation based on canonical gene expression pattern and copy number variations (CNVs), we identified 360,214 single cells organized into 12 main lineages (Figures S1A, S1B, Tables S2, and S3). The two most abundant cell types were tumor cells (46% of the total) and myeloid cells (30% of the total) (Figure S1A). Myeloid cells were further clustered into monocytes, Mo-TAMs, Mg-TAMs, dendritic cells (DCs), and proliferative TAM based on canonical cell type markers (Figures 1, S1C, and Table S3).¹⁵ Intriguingly, the proportion of Mo-TAM in GBM-IDHwt was higher than IDH-mutant gliomas (Astro-IDHmut and Oligo-IDHmut), whereas Mg-TAM was more prevalent in IDH-mutant gliomas compared with GBM-IDHwt (Figure S1D). We further subclustered Mg-TAMs and DCs into different cellular states or subtypes, resulting in five states of Mg-TAMs and four subtypes of DCs that underscore the transcriptional diversity within each type of tumor-infiltrating myeloid cells (Figures S1E–S1G).

Mo-TAM clusters across diffuse gliomas are largely conserved but with remarkable differences in cellular composition

To determine the heterogeneity of Mo-TAM clusters in diffuse gliomas, we dissected human Mo-TAMs and identified six clusters exhibiting distinctive molecular features (Figures 1C–1E, and

Figure 1. Single-cell landscape of Mo-TAMs in diffuse gliomas in human

- (A) Experimental workflow. PDX, patient-derived xenografts.
- (B) Locations of human glioma specimens in our scRNA-seq dataset.
- (C) Uniform manifold approximation and projection (UMAP) plot showing different types of myeloid cells ($n = 105,839$ cells) and Mo-TAM clusters ($n = 30,864$ cells) across 31 human glioma specimens from our scRNA-seq dataset. Prol.TAM, proliferative TAM.
- (D) Dot plots of cell-specific markers. Avg.exp, average expression.
- (E) Gene set variation analysis (GSVA) across Mo-TAM clusters. NES, normalized enrichment score.
- (F) UMAP plots of Mo-TAM clustering using our GL261 mGBM scRNA-seq dataset ($n = 4$ cases).
- (G) Non-negative least-squares regression (NNLS) analysis showing the similarity of Mo-TAM clusters between hGBMs (horizontal axis) and mGBMs (vertical axis).
- (H) Boxplots showing the frequency of different Mo-TAM clusters in hGBM-IDHwt ($n = 20$ cases), hAstro-IDHmut ($n = 8$ cases), and hOligo-IDHmut ($n = 3$ cases) from our scRNA-seq dataset. Center line shows median, box limits indicate upper and lower quartiles, and whiskers extend 1.5 times the interquartile range; two-sided unpaired Wilcoxon test. *, $p < 0.05$. ns, not significant.
- (I) Stacked barplot of cell composition of myeloid cell types (left panel) and Mo-TAM clusters (right panel) across hGBM ($n = 40$ cases) and mGBM ($n = 12$ cases). See also Figures S1 and S2 and Tables S1–S3.

Table S3). Specifically, the Hypoxia-TAM cluster exhibited prominent hypoxia response programs characterized by the upregulation of hypoxia response genes (*ADM*, *BNIP3*, and *CSTB*), enhanced glycolysis, and proangiogenic features. The chemotaxis (Chemo)-TAM cluster was featured by gene modules involved in cell migration and leukocyte chemotaxis. The interferon (IFN)-TAM cluster displayed upregulation of IFN-stimulated genes (*IFIT1*, *IFIT3*, and *IFI44L*) and an IFN-response signature (*CXCL10*, *MX1*, and *MX2*). The Lipid-TAM cluster was characterized by enriched lipid metabolism and upregulation of lipid carrier proteins (*APOC1* and *APOE*). The ribosome (Ribo)-TAM cluster was enriched for ribosomal genes (*RPL13* and *RPL19*) and featured by rRNA processing program. The phagocytosis and antigen presentation (Phago/AP)-TAM cluster was recognized by the upregulated genes involved in phagocytosis and antigen presentation (*CD83* and *HLA-DRA*) (Figures 1D and 1E). None of these Mo-TAM clusters showed CNVs (Figure S2A). Meta-analyses of public scRNA-seq datasets of hGBM^{28–30} and mGBM¹⁸ confirmed that Mo-TAM clusters were largely conserved (Figures 1F–1I and S2B–S2D). However, the composition of Mo-TAMs significantly varied across different types of diffuse gliomas in human. Higher frequencies of Hypoxia-TAM and Chemo-TAM and a lower proportion of Phago/AP-TAM were found in GBM-IDHwt than IDH-mutant gliomas (Figure 1H).

To investigate the relevance of the Mo-TAM clustering strategy in other tumors, we employed public scRNA-seq datasets of breast carcinoma (BRCA), colorectal carcinoma (CRC), lung adenocarcinoma (LUAD), and hepatic cell carcinoma (HCC) in human.^{31–34} The transcriptomic profiles of Hypoxia-TAM, IFN-TAM, and Lipid-TAM appeared to be largely conserved across different tumor types (Figure S2E). By contrast, the presence of Phago/AP-TAM, Ribo-TAM, or Chemo-TAM was tumor context dependent (Figure S2E). Mo-TAM clustering in these tumors also suggested the presence of other Mo-TAM subsets that cannot be classified as those identified in diffuse gliomas (Figure S2E). These data provide insights into intra- and inter-tumoral heterogeneity of the Mo-TAM pool across diffuse gliomas and other tumors in human.

Clinical implications of Mo-TAM composition across diffuse gliomas

Using The Cancer Genome Atlas (TCGA)-GBM/low-grade glioma RNA sequencing (RNA-seq) dataset, we investigated the translational significance of the Mo-TAM clustering scheme. The frequency of each Mo-TAM cluster was estimated using deconvolution analysis. The frequencies of Hypoxia-TAM, Chemo-TAM, IFN-TAM, and Lipid-TAM increased, whereas those of Ribo-TAM and Phago/AP-TAM decreased in GBM-IDHwt compared with IDH-mutant gliomas (Figures 2A and 2B). The proportions of different Mo-TAM clusters were also associated with glioma grades (Figure 2A) and key molecular changes (Figures 2C and 2D) using TCGA samples. Strikingly, the estimated proportion of Hypoxia-TAM independently indicated a worse outcome in patients with GBM (Figure 2E), suggesting its tumor-supportive function. These data highlight the feasibility and replicability of the Mo-TAM classification scheme for evaluating Mo-TAM composition in diffuse gliomas with clinical implications.

The cellular diversity of Mo-TAMs at the spatial resolution

To spatially resolve the heterogeneity of Mo-TAMs, we contextualized the transcriptional signature of Mo-TAMs to different histological regions of hGBM tissues using the Ivy-hGBM cohort and estimated the proportion of each Mo-TAM cluster (Figure 3A). Notably, Hypoxia-TAM was preferentially localized in the peri-necrotic region. The proportion of IFN-TAM was relatively high in the peri-vascular region. Chemo-TAM was decreased, whereas Ribo-TAM and Phago/AP-TAM were modestly increased in the infiltrating tumor region. By contrast, the proportion of Lipid-TAM showed variation across regions and samples (Figure 3A). To delineate Mo-TAM transcriptional diversity at the spatial level, we reanalyzed public hGBM spatial transcriptomic datasets^{20,21,35} and integrated transcriptional patterns of Mo-TAMs with histological characteristics of hGBM. Spatially resolved transcriptomic profiling largely recapitulated the predicted spatial distribution of different Mo-TAM clusters in Ivy-hGBM cases (Figures 3B–3D, and S3A).

Hypoxia gradient and associated cellular features mapped on hGBM tissues

GBM features a profoundly hypoxic niche. To delineate cellular composition associated with hypoxia, we mapped the spatial gradient of hypoxia in hGBM tissues using public spatial transcriptomic datasets (Figure S3B). The hypoxia regions and neighborhood zones were defined based on the scoring of hypoxia feature in each spot and were graded into five hypoxia levels (Figure S3C). The proportion of Hypoxia-TAM was upregulated along with increased hypoxia gradient, whereas that of other Mo-TAM clusters was decreased (Figure S3D). Intriguingly, increased hypoxia level was also associated with enrichment of mesenchymal states (MES1/2) of hGBM cells (Figure S3E). Functionally, cells in the hypoxic niche were featured by augmented cell death, angiogenesis, senescence, and glycolysis in response to hypoxia,²⁴ as well as repressed cell cycling and oxidative phosphorylation (Figure S3F). Moreover, increased hypoxia gradient was associated with suppressed immune activity of macrophages and T cells, as well as mitigated DNA repair capacity that contributes to genomic instability and drug resistance (Figure S3G).

Specified analysis of the spatial feature of Hypoxia-TAM revealed that the Hypoxia-TAM transcriptional signature and expression of *ADM* as a marker gene were markedly upregulated in the hypoxic tumor regions (Figure S4A). Co-staining for *ADM* and the Mo-TAM marker galectin-3¹⁶ confirmed the proximity of Hypoxia-TAM (defined as *ADM*⁺/Galectin-3⁺ Mo-TAMs) to the pseudo-palisading necrotic areas in hGBM tissues (Figures 3E, S4B and S4C). Consistently, the expression of Hypoxia-TAM signature genes was significantly upregulated in hGBMs compared with low-grade gliomas (Figure S4D). These data confirm the enrichment of Hypoxia-TAM in the hypoxic niche of hGBMs.

Hypoxic tumor cues induce Hypoxia-TAM polarization

To determine whether the polarization of Hypoxia-TAM could be driven by hypoxic tumor cues, we established an *in vitro* Mo-TAM polarization model (Figure 4A). The culture condition of hGBM-3 tumor cell-conditioned medium (TCM) plus 1% O₂

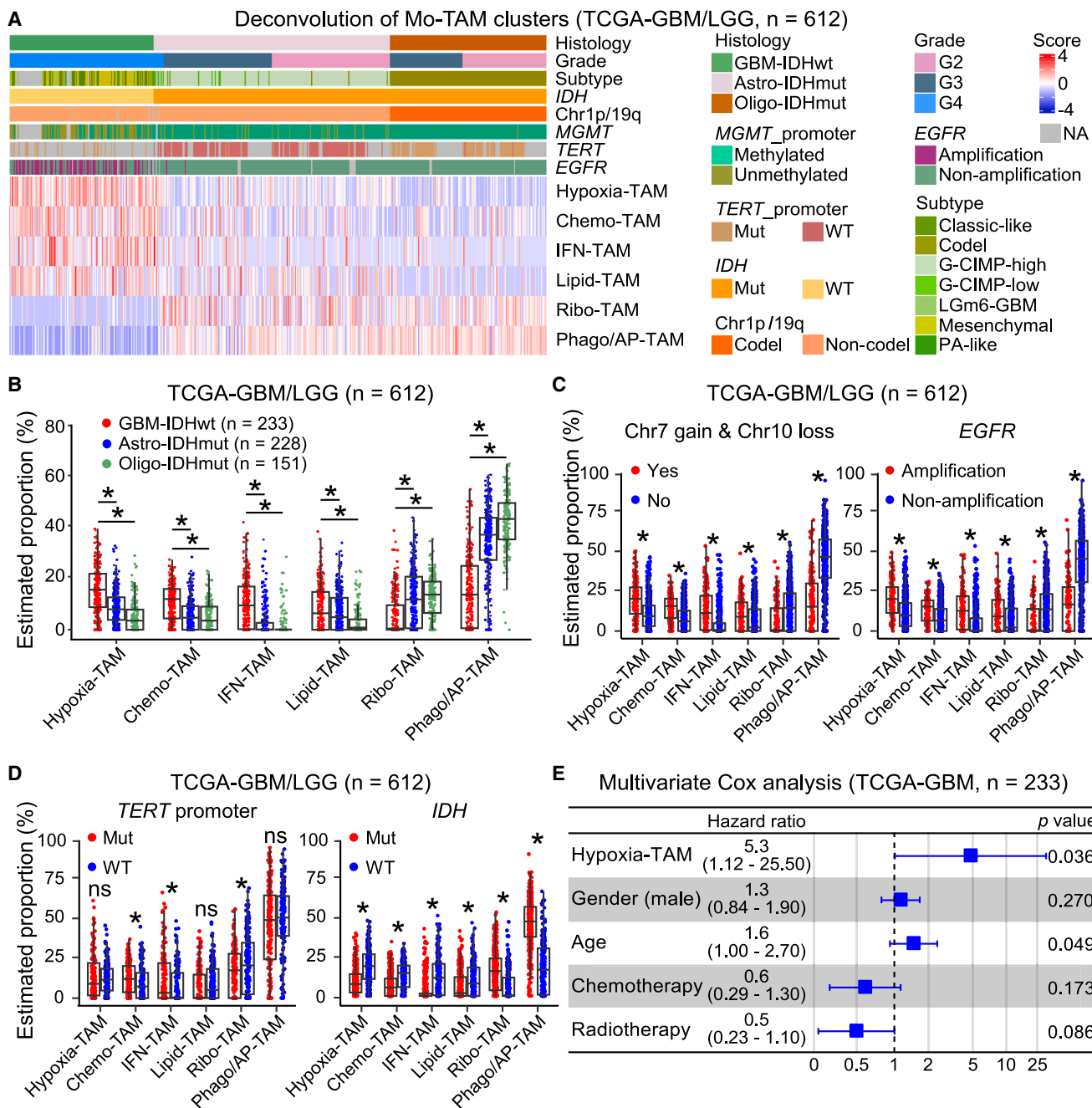


Figure 2. Clinical relevance of the Mo-TAM classification scheme

(A) Heatmap depicting the estimated proportions of different Mo-TAM clusters across diffuse gliomas using TCGA-GBM/LGG cohort ($n = 612$ cases). LGG, low-grade gliomas. *MGMT*, O6-methylguanine-DNA methyltransferase. *EGFR*, epidermal growth factor receptor. *TERT*, telomerase reverse transcriptase. Chr, chromosome. Codel, co-deletion. G-CIMP, glioma-CpG island methylator phenotype. PA-like, pilocytic astrocytoma-like. LGm6-GBM is a subgroup of glioma enriched for histologic low-grade gliomas and contains a subset of tumors with GBM-defining histologic criteria. NA, not applicable.

(B-D) Boxplots showing the estimated proportions of Mo-TAM clusters across diffuse gliomas with different types (B) or molecular signatures (C and D) using TCGA-GBM/LGG cohort ($n = 612$ cases). Center line shows median, box limits indicate upper and lower quartiles, and whiskers extend 1.5 times the interquartile range. *, $p < 0.05$. ns, not significant. Two-sided unpaired Wilcoxon test.

(E) Multivariate Cox regression analysis of the overall survival of patients using TCGA-GBM cohort ($n = 233$ cases). Forest plots with error bars show 2.5% (lower) and 97.5% (higher) bounds of the confidence interval.

effectively upregulated the expression of Hypoxia-TAM signature genes in Mo-TAMs derived from human peripheral blood mononuclear cells (PBMCs), U937 cells, and mouse bone-

marrow-derived macrophages (BMDMs) (Figures 4B, S5A and S5B). We performed bulk RNA-seq of macrophages ($M\varphi$) under the stimulation of TCM and/or 1% O_2 (Figure S5C). Evaluation of

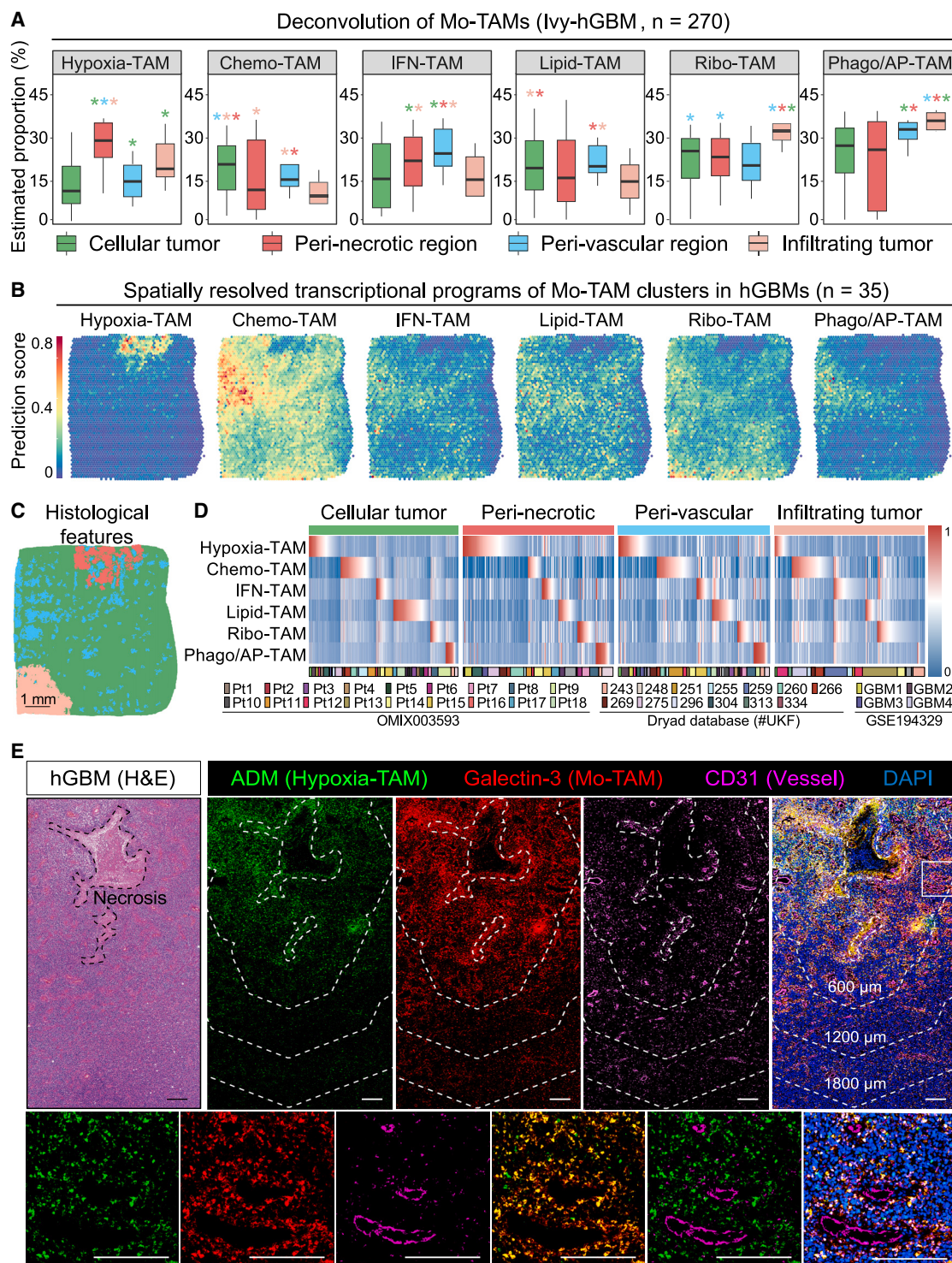


Figure 3. Cellular diversity of Mo-TAMs at the spatial resolution

(A) Boxplots showing the estimated proportions of Mo-TAM clusters across different histological regions of hGBMs using bulk RNA-seq data from the Ivy-hGBM cohort ($n = 270$ cases). Estimated cell proportion of clusters with overhead asterisk differs from that of clusters with corresponding asterisk color. *, $p < 0.05$. Two-sided unpaired Wilcoxon test.

(B) Surface plots showing the transcriptional programs across Mo-TAM clusters at spatial resolution using three public hGBM spatial transcriptomic datasets ($n = 35$, Case #275 is presented).

(C) The annotated histological features of hGBM (Case #275). Scale bar, 1 mm.

(legend continued on next page)

expression of the Hypoxia-TAM signature genes in these four differentially polarized bulk M ϕ indicated that M ϕ exposed to TCM plus 1% O₂ largely resembled Hypoxia-TAM transcriptional signature annotated in our hGBM scRNA-seq dataset, whereas M ϕ treated with either TCM or 1% O₂ partially recapitulated Hypoxia-TAM feature (Figure S5D). To clarify the roles of tumor-induced changes versus hypoxia-induced changes on Hypoxia-TAM polarization, we screened for tumor cell-produced factors using quantitative proteomics analysis of TCM and evaluated changes of glycolytic metabolite spectrum under hypoxia stimulation (Figures S5E and S5G). Tumor cell-derived secreted protein acidic and rich in cysteine (SPARC) (Figure S5F) and hypoxia-induced lactate (Figure S5H) were identified as critical niche factors for inducing Hypoxia-TAM signature, the combination of which largely resembled hypoxic tumor cues for Hypoxia-TAM polarization (Figures S5I–S5K).

To uncover Mo-TAM phenotypic changes steered by hypoxic tumor cues, we screened for hypoxia positively or negatively correlated genes (termed HPGs or HNGs) using hGBM scRNA-seq data and mapped hypoxia-associated gene interaction network. The upregulated programs were associated with TAM recruitment (MES-like cell migration), cell adaptation to hypoxia (starvation, autophagy, and glycolysis), and niche remodeling (angiogenesis and extracellular matrix degradation) (Figure 4C). The downregulated programs resembled immunosuppressive features of TAMs (impaired phagocytosis, retarded antigen presentation, inefficient T cell activation, and reduced IFN production) and cell-cycle arrest (Figure 4C). Core transcription factors (TFs) and hypoxia response genes were enriched in the Hypoxia-TAM cluster and closely connected with the aforementioned programs (Figure 4C).

p50 transactivates Hypoxia-TAM signature genes

To uncover the intracellular pathways mediating Hypoxia-TAM polarization, we performed bulk RNA-seq of PBMC-derived M ϕ exposed to hGBM-3-TCM (M ϕ -TCM), 1% O₂ (M ϕ -hypoxia), or both (Hypoxia-TAM). Gene set enrichment analysis (GSEA) of the M ϕ bulk RNA-seq data revealed the nuclear factor kappa B (NF-κB) signaling as the most significantly upregulated pathway in Hypoxia-TAM compared with M ϕ , which was also enriched in M ϕ exposed to TCM (M ϕ -TCM) or 1% O₂ (M ϕ -hypoxia) (Figure S6A). We also screened for the potential TFs regulating Hypoxia-TAM signature using single-cell regulatory network inference and clustering (SCENIC) analysis of hGBM scRNA-seq data (Figure S6B). Subsetting for the top 10 TFs with the highest regulon activity score for the Hypoxia-TAM cluster and a hypoxia response geneset from the GSEA Molecular Signatures Database (MSigDB) suggested p50, hypoxia-inducible factor-1 α (HIF1 α), and c-Jun as core TFs regulating Hypoxia-TAM signature (Figure 4D). To determine whether p50, HIF1 α , and c-Jun are required for the upregulated expression of Hypoxia-TAM signature genes, we used short hairpin RNAs (shRNAs) to specifically knock down these TFs in PBMC-derived Hypoxia-TAM (Figure S6C, and Table S6). Disruption of p50 (encoded

by *NFKB1*), but not the other two TFs, markedly decreased the expression of Hypoxia-TAM signature genes (Figures 4E and S6D). These results suggest that p50 as a downstream TF of NF-κB signaling is required for Hypoxia-TAM signature.

To address whether p50 responses to the extrinsic stimuli from tumor cells or hypoxia, we determined p50 nuclear translocation, and found a partial increase of p50 nuclear signal in M ϕ -TCM and M ϕ -hypoxia and a more pronounced p50 nuclear signal in Hypoxia-TAM versus control M ϕ derived from PBMCs (Figures S6E and S6F). Similarly, treatment of recombinant human SPARC (rhSPARC) and lactate effectively induced p50 nuclear translocation (Figure S6G), the effect of which was largely compromised when their functions were perturbed using pharmacological approaches (Figure S6H). We also confirmed p50-mediated transcription of *ADM* as a Hypoxia-TAM signature gene (Figures 4F–4H). These findings indicate that tumor cell-produced SPARC and hypoxia-induced lactate concertedly promote Hypoxia-TAM polarization at least in part through activating p50 (Figure 4I).

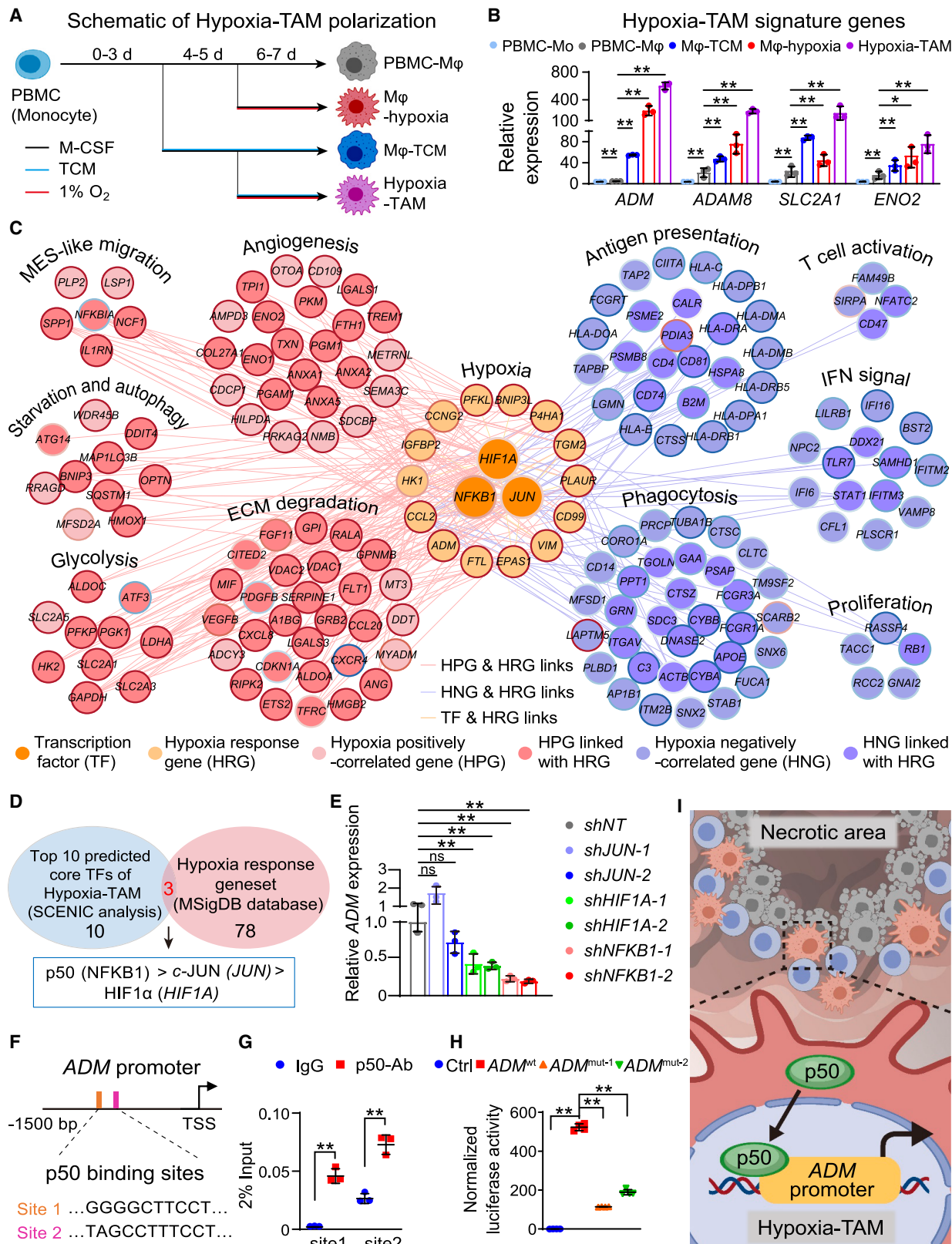
Genetic ablation of *Adm* restores mGBM vascular integrity

We determined the functional significance of Hypoxia-TAM in the hypoxic niche. In the peri-necrotic region of hGBM, enriched Hypoxia-TAM was accompanied by abundant microvessels (Figure 3E). Gene set variation analysis using hGBM scRNA-seq data revealed that Hypoxia-TAM was enriched for pathways regulating vasculature integrity and development (Figure 5A). This prompted us to identify Hypoxia-TAM-derived factors that may reshape tumor vasculature. Subsetting for Hypoxia-TAM signature genes using hGBM scRNA-seq dataset, human genes that encode secreted proteins,³⁶ and a hypoxia response geneset from MSigDB revealed *ADM* as the only candidate (Figures 5B and S7A). We conditionally knocked out *Adm* in monocyte derivatives using *Ccr2-Cre-eGFP*; *Adm*^{f/f} mice (termed *Adm* cKO mice) (Figure S7B) and established GL261 mGBM xenografts (Figure 5C). *Adm* knockout efficacy was confirmed in BMDM-derived TAMs (Figure S7C) and the *Adm* cKO xenografts (Figures S7D and S7E).

Intravital imaging of dextran (70 kDa)-labeled tumor vasculature revealed moderately decreased tumor vessels and join point density in the *Adm* cKO xenografts compared with the *Ccr2-Cre-eGFP* (WT) xenografts (Figures 5D and 5E). Structurally, compared with the wide gaps between adjoining endothelial cells (ECs) in the WT xenografts, those in the *Adm* cKO xenografts were substantially narrowed (Figure 5F). Immunostaining showed that expression of the endothelial adherens junction marker vascular endothelial (VE)-cadherin³⁷ was largely restored in the *Adm* cKO xenografts (Figures 5G and S7F). Meanwhile, expressions of the tight junction marker claudin-5, pericyte marker platelet-derived growth factor receptor beta, and vascular basement membrane marker laminin were unaffected by *Adm* knockout (Figures 5G and S7G–S7I). Evaluation of tumor vascular permeability using

(D) Heatmap of spatially resolved hGBM transcriptomics arranged by distinct histological regions using public hGBM datasets ($n = 35$ cases). Sample numbers are illustrated below the heatmap.

(E) H&E staining and immunostaining of ADM, galectin-3, and CD31 in the peri-necrotic region of hGBMs. Dashed lines indicate the distances (600 μ m/line) from necrotic cores. An area indicated with a square is enlarged and shown in each color or the combination of different colors at the bottom. Scale bar, 200 μ m. See also Figures S3 and S4.



(legend on next page)

cadaverine (1 kDa) revealed a substantial reduction of cadaverine effusion areas in the *Adm* cKO xenografts versus the WT xenografts (Figures 5G and S7J). In contrast, vascular integrity and permeability in mouse normal brains remained unaffected by *Adm* knockout (Figures S7K–S7M). These data demonstrate that *Adm* knockout selectively restores tumoral vessel integrity and decreases vascular leakage in mGBM xenografts.

ADM activates CRLR-VE-cadherin signaling to destabilize endothelial adherens junctions

Enrichment of the adherens junction pathway and increased expression of VE-cadherin encoding gene *Cdh5* were observed in ECs derived from the *Adm* cKO xenografts compared with the WT xenografts (Figures S7N and 6A). To determine how ADM impairs endothelial adherens junctions, we treated human brain microvascular ECs (HBMECs) with recombinant human ADM (rhADM) and found that membrane VE-cadherin translocated to the cytoplasm (Figure 6B). Consistently, apparent separation of endothelial junctions and internalization of VE-cadherin were observed in HBMECs receiving U937 Hypoxia-TAM-derived conditioned medium (TAM-CM), which was largely rescued by AMA treatment (Figures 6C and 6D). Consequently, vascular leakage, as detected by fluorescein-streptavidin dye, was increased in HBMECs receiving TAM-CM, but was reduced in those receiving AMA (Figures 6C and 6D).

To uncover how EC responds to ADM, we inferred interaction between ADM and its receptors²⁷ using CellphoneDB analysis of hGBM scRNA-seq data and identified an enhanced interaction of ADM-CRLR between Hypoxia-TAM and EC (Figure 6E). Immunostaining confirmed the colocalization of CRLR and the EC marker CD31 with upregulated ADM signal in the peri-necrotic region of hGBM (Figures 6F and 6G). Functionally, silencing CRLR expression using shRNAs largely compromised ADM-induced VE-cadherin internalization and vascular leakage (Figures 6H and 6I). As an intracellular downstream cascade, phosphorylation of Src³⁸ and VE-cadherin³⁹ and subsequent VE-cadherin internalization were markedly increased upon Hypoxia-TAM-CM stimulation, whereas AMA treatment largely abrogated this signaling activation (Figure 6J). Consistently, CRLR disruption in HBMECs largely compromised rhADM-induced phosphorylation of Src and VE-cadherin (Figure 6K). These results demonstrate that ADM secreted by Hypoxia-TAM activates CRLR signaling in ECs, thereby disrupting VE-cadherin-mediated adherens junctions (Figure 6L).

Figure 4. Hypoxic tumor cues promote Hypoxia-TAM polarization

- (A) Schematic illustration of monocyte polarization toward different states of Mφ. TCM was derived from hGBM-3.
- (B) qRT-PCR analysis of expression of Hypoxia-TAM signature genes (*n* = 3 samples/group). Mo, monocytes.
- (C) Network diagram illustrating the hypoxia-associated gene interactions and pathway enrichment for Hypoxia-TAM. Core TFs regulating hypoxia response programs are denoted as orange circles. Gene interactions across HRGs (yellow), HPGs (red), and HNGs (blue) are denoted by lines with corresponding colors. ECM, Extracellular matrix.
- (D) Subsetting of the predicted core TFs for Hypoxia-TAM and a hypoxia response geneset.
- (E) qRT-PCR analysis of *ADM* expression in PBMC-derived Hypoxia-TAM expressing shRNAs targeting *JUN*, *HIF1A*, and *NFKB1* (*n* = 3 samples/group).
- (F) Schematic illustration of p50 binding sites on the *ADM* gene promoter. TSS, transcription start site.
- (G) ChIP-qPCR of p50 using PBMC-derived Hypoxia-TAM (*n* = 3 samples/group). Ab, antibody.
- (H) Luciferase reporter analysis conducted in PBMC-derived Hypoxia-TAM (*n* = 4 samples/group). Hypoxia-TAM was transfected with luciferase vectors containing *ADM* promoter region with the wild-type binding site (*ADM*^{WT}) or mutant binding sites (*ADM*^{mut-1, -2}) of p50.
- (I) Schematic illustration of p50-mediated *ADM* transcription in Hypoxia-TAM. Data in all quantitative panels are displayed as mean ± SD; two-way ANOVA (B, E, and H), and two-tailed unpaired t test (G). ns, not significant. *, *p* < 0.05. **, *p* < 0.01.

See also Figures S5 and S6.

Enhanced ADM expression is associated with tumor vessel hyperpermeability in hGBM

Upregulation of ADM in hGBMs was associated with reduced VE-cadherin expression in tumor vessels (Figures 7A, 7B, and Table S4), supporting ADM-mediated endothelial junction destabilization. GSEA indicated that patients with high level of *ADM* harbored hyperpermeable tumor vessels that dampen drug delivery (Figure S8A).⁴⁰ Consequently, increased *ADM* expression predicted worse outcomes for patients receiving chemotherapy (Figure S8B), which might be associated with low perfusion of drugs into tumors.

Targeting ADM through AMA for normalizing tumor vessels

Stabilization of endothelial junctions is deemed as a central part for preserving vascular integrity in brain tumors.⁴¹ Therefore, we determined whether blocking ADM through AMA could restore endothelial adherens junctions. To this end, we established hGBM-3 xenografts co-implanted with U937-derived TAMs (Figure 7C, and Table S5).⁴ This model successfully mimicked the histology of the hypoxic niche in hGBMs, including tumor necrosis, neovasculature with impaired adherens junctions, and infiltration of ADM-producing TAMs (Figures S8C–S8E). We confirmed ADM-induced CRLR signaling activation in mouse ECs (Figure S8F). Strikingly, AMA administration restored VE-cadherin expression, preserved endothelial junctions, and reduced cadaverine effusion in hGBM-3 xenografts co-implanted with U937-derived TAMs, but had negligible influence on mouse normal brain vasculature (Figures 7D and 7E; S8G). Consequently, AMA treatment reduced tumor hypoxia and enhanced drug delivery, as demonstrated by the substantial decrease in the pimonidazole-labeled hypoxic areas and the increase in the doxorubicin-perfused areas in xenografts receiving AMA (Figures 7F–7I). Magnetic resonance imaging confirmed increased blood perfusion in GL261 mGBM xenografts receiving AMA (Figures S8H–S8J).

Additionally, ADM stimulation did not alter hGBM-3 cell viability (Figure S8K), suggesting that the primary consequence of ADM blockade is restoring tumor vascular integrity. To confirm that the main microenvironmental source responsible for vascular hyperpermeability is TAM-secreted ADM, we constructed control hGBM-3 xenografts without implantation of U937-derived TAMs and found that AMA administration had minimal impact on VE-cadherin expression and cadaverine effusion (Figure S8L). Consistently, no apparent difference of the pimonidazole-labeled

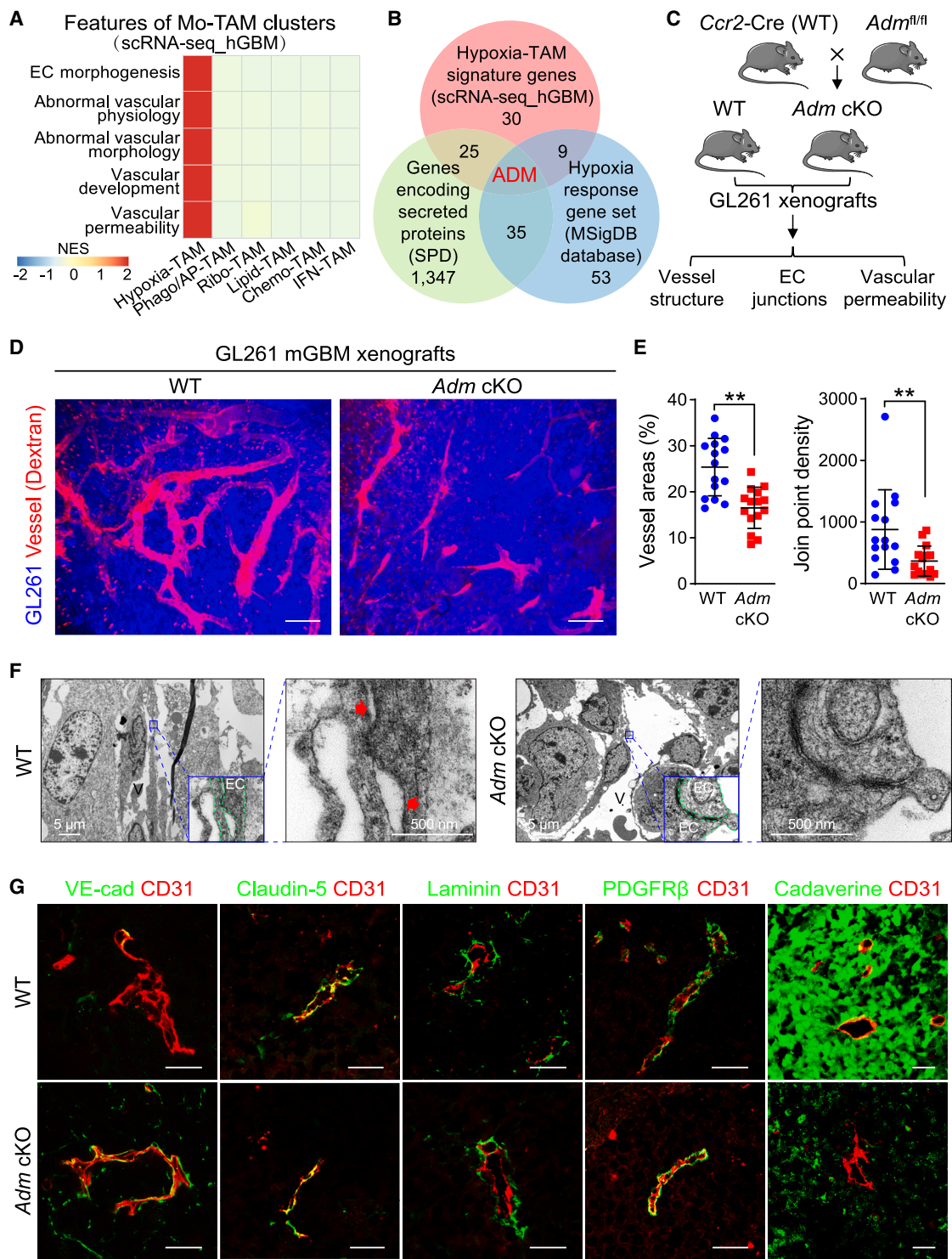


Figure 5. Adm knockout restores vascular integrity in mGBM xenografts

(A) GSVA of hGBM scRNA-seq data showing pathways enriched for Hypoxia-TAM.

(B) Subsetting of the Hypoxia-TAM signature genes from our hGBM scRNA-seq dataset, secreted protein-encoding genes from web-based secreted protein database (SPD), and a hypoxia response genes set from MSigDB.

(C) Schematic illustration of generation of the *Ccr2-Cre-eGFP* (WT) mice and *Adm* cKO mice and subsequent evaluation of tumor vessels in GL261 mGBM xenografts.

(D and E) Intravital imaging of dextran-labeled tumor vasculature (D) and quantification of vessel structure (E) in the WT and *Adm* cKO xenografts ($n = 15$ images/group). Scale bar, 100 μ m. Data are shown as mean \pm SD; two-tailed unpaired t test. **, $p < 0.01$.

(legend continued on next page)

hypoxic areas or the doxorubicin-perfused areas was found between the control hGBM-3 xenografts treated with AMA or vehicle (Figure S8M). These results support that ADM derived from TAM is critical for disrupting tumor vasculature.

AMA improves drug delivery and therapeutic efficacy of dabrafenib

The potent effect of AMA in restoring tumor vascular integrity prompted us to investigate whether its combination with anti-tumor agents could achieve synergistic therapeutic benefits. Dabrafenib is a brain-penetrating BRAF kinase inhibitor for treating BRAF^{V600E}-mutant brain tumors.^{42,43} The low intratumoral concentration of dabrafenib thwarts its therapeutic efficiency,⁴³ partially owing to hyperpermeable neovasculature in brain tumors. BRAF^{V600E}-mutant hGBMs (Table S4) exhibited apparent necrosis, abundant vessels with a paucity of VE-cadherin, and extensive ADM-producing TAMs (Figures 8A and 8B). Mice bearing BRAF^{V600E}-mutant hGBM-4 xenografts (Table S5) received one of the four therapeutic arms, namely vehicle control, AMA, dabrafenib, or a combination of AMA and dabrafenib (Figure 8C). AMA administration with dabrafenib achieved combinatorial therapeutic benefits in extending animal survival (Figure 8D) and reducing tumor burden (Figures 8E and 8F). Moreover, AMA treatment substantially increased the proportion of VE-cadherin-expressing vessels, reduced cadaverine leakage, and increased intratumoral dabrafenib concentration (Figures 8G–8I). The combinatorial therapeutic efficacy was confirmed by the substantial decrease in phosphorylated extracellular signal-regulated kinase (p-ERK)⁺ cells and the increase in terminal deoxynucleotidyl transferase dUTP nick end labeling (TUNEL)⁺ apoptotic cells in xenografts receiving dabrafenib and AMA compared with those receiving vehicle control or each monotherapy (Figures 8J and 8K). Collectively, our results provide preclinical evidence for leveraging AMA as a vascular normalizing agent to improve the delivery and therapeutic efficacy of anti-tumor drugs.

DISCUSSION

Distinct tumor niche-specific cues skew monocyte differentiation and induce discrete Mo-TAM phenotypes to support tumor progression.¹² This study charted a spatially resolved transcriptomic landscape of Mo-TAMs across diffuse gliomas. Mo-TAM clusters were largely conserved, but their composition varied among GBM-IDHwt and IDH-mutant gliomas, among IDH-mutant gliomas of different grades and even among different histological regions within the same GBM. Evaluation of the cellular composition of Mo-TAM clusters using scRNA-seq or bulk RNA-seq could be exploited to predict the tumor type, grade, histological features, and patient prognosis of diffuse gliomas. Moreover, our work delineates the functionality of Mo-TAMs by integrating single-cell multi-omics data and functional approaches, thereby shedding light on potential immunotherapies targeting distinct clusters within the TAM pool.

Hypoxia is a hallmark of GBM. TAMs can be recruited to the hypoxic tumor niche to fuel glioma progression and therapeutic resistance.^{25,26} These findings necessitate the need to specify how hypoxic niche cues skew TAM phenotype. We identified Hypoxia-TAM as a distinct Mo-TAM cluster enriched in the hypoxic niche of GBMs and shaped by hypoxic tumor cues to stimulate neovascularization. This is evidenced by (1) the conserved transcriptional signature of Hypoxia-TAM found in GBM tissues of humans and mice *in situ* and cell models *in vitro*, (2) the identification of a p50-triggered hypoxia response program as a fundamental mechanism underlying Hypoxia-TAM polarization, and (3) the role of Hypoxia-TAM in inducing tumor vessel resilience, augmented MES-like cell migration, impaired T cell activation, and increased degradation of extracellular matrix, which could be associated with hypoxia stress as a driving force.^{25,44} Previous studies corroborate our findings by revealing preserved TAM subsets sharing hypoxia response signatures in other solid tumors.^{19,45} Whether the Hypoxia-TAM phenotype switch is related to tumor stages, and how hypoxic niche cues induce a concerted action of Hypoxia-TAM and other tumor components to sustain GBM as an ecosystem require further investigation.

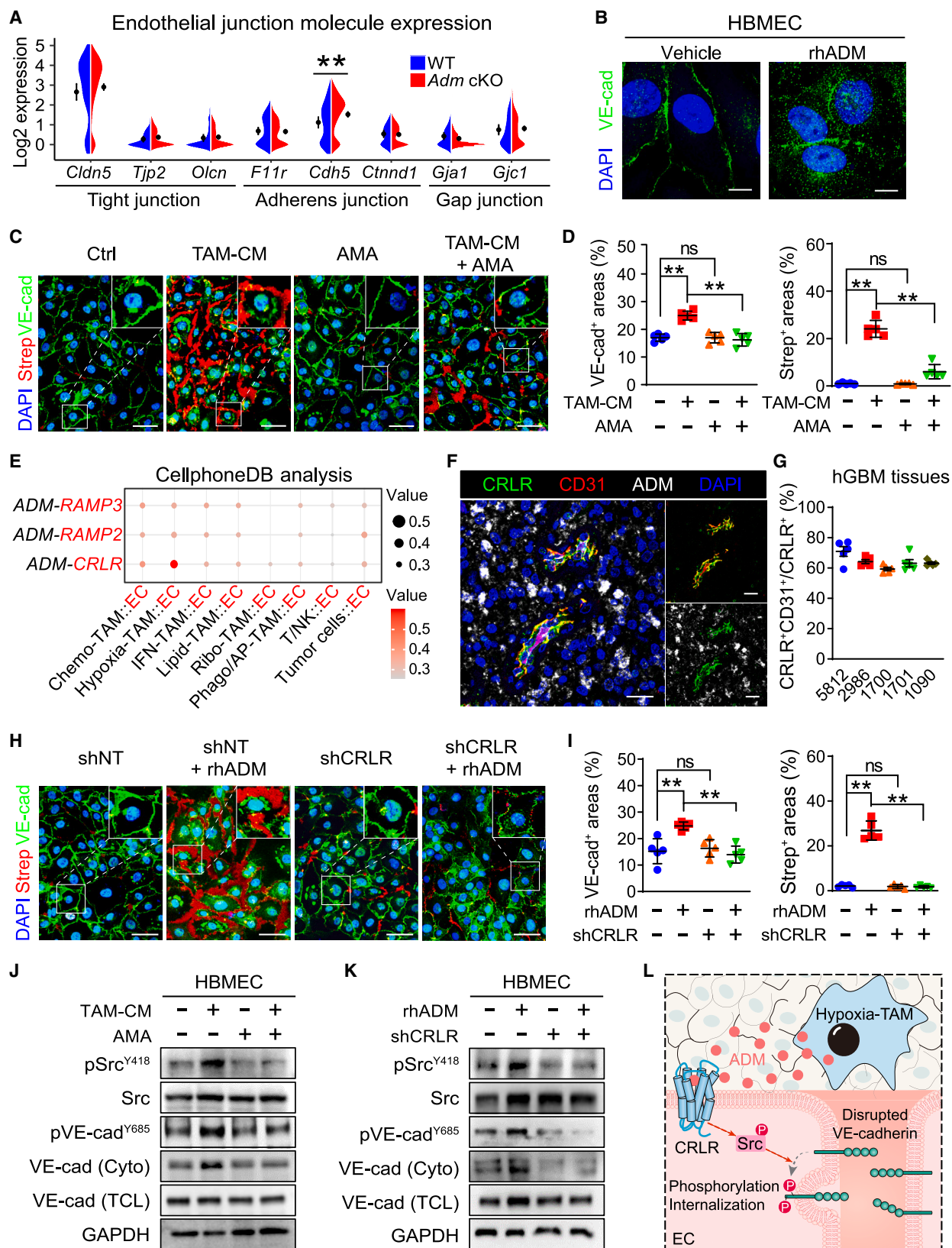
The hypoxic niche of GBMs is surrounded by abundant but structurally destabilized blood vessels that severely retard blood perfusion and drug delivery.^{40,46} To date, the direct effect of TAMs on the vascular structural integrity of GBMs remains poorly characterized. We report Hypoxia-TAM as a direct contributor to hyperpermeable tumor vessels, ADM as an orchestrator of destabilized endothelial connections, and the VE-cadherin adhens junction as an important structural basis for restoring tumor vascular integrity. Our findings, together with emerging insights into the manipulation of the structure of tumor vessels,⁴⁷ may lead to new strategies for normalizing tumor vasculature. Indeed, pharmacological perturbation of ADM stabilizes endothelial junctions in tumor vessels, but has a negligible impact on vessels in normal brains, underscoring ADM as a selective and druggable target. Notably, the blockade of ADM for re-establishing a stabilized vascular structure differs from focused ultrasound therapy that focuses on increasing local vascular permeability through opening the blood-tumor barrier,⁴¹ and may avoid the adverse consequences of ultrasound therapy including edema, hemorrhage, and high interstitial pressure that impede blood flow into brain tumors. Further investigations are warranted to determine whether ADM antagonists or neutralizing antibodies⁴⁸ could be leveraged as alternatives for normalizing tumor vasculature in other tumors with elevated ADM expression.

Many potent anti-tumor agents are ineffective against GBM due to limited drug delivery. We showed that the administration of AMA enhanced anti-tumor drug perfusion, thereby expanding the spectrum of anti-GBM drugs. Indeed, AMA in combination with anti-tumor agent dabrafenib improved drug concentration in orthotopic hGBM xenografts and achieves better therapeutic efficacy with ensuing survival benefits. Since destabilized vasculature and its associated poor drug delivery are common across brain tumors, the application of AMA may extend beyond GBM

(F) Transmission electron microscopy (TEM) of microvessels in xenografts ($n = 15$ images/group). ECs and gaps between them are highlighted by green dashed lines and red arrows, respectively. V, vessel. Scale bar, 5 μm (left panels) or 500 nm (right panels).

(G) Immunostaining of VE-cadherin, claudin-5, laminin, PDGFR β , cadaverine, and CD31 in xenografts ($n = 15$ images/group). Scale bar, 25 μm .

See also Figure S7.



(legend on next page)

treatment, particularly when combined with dabrafenib for treating primary and metastatic brain tumors driven by BRAF^{V600E} mutation.^{42,43} In addition, recent advances suggest an association between abnormal tumor vasculature and decreased infiltration or activity of immune cells.^{40,47} AMA-induced vascular normalization may extend to the potentiation of immunotherapy.

In conclusion, we chart the landscape of Mo-TAMs in diffuse gliomas, characterize the molecular and functional signature of the Hypoxia-TAM subset in hypoxic tumor niche, and underscore its prognostic and therapeutic implications. Beyond the Mo-TAM subsets characterized in this study, exceptions remain in patients with diffuse gliomas under specific scenarios, such as tumor stages, recurrence status, and responses to specific therapies. Additional studies remain warranted to ascertain distinctions between isolated Mo-TAM clusters and the continuous spectrum of cell states. Nevertheless, our work provides a rationale for characterizing functionally discrete Mo-TAM clusters and developing new targeted therapies.

STAR★METHODS

Detailed methods are provided in the online version of this paper and include the following:

- KEY RESOURCES TABLE
- RESOURCE AVAILABILITY
 - Lead contact
 - Materials availability
 - Data and code availability
- EXPERIMENTAL MODEL AND SUBJECT DETAILS
 - hGBM specimens
- EXPERIMENTAL MOUSE MODELS
 - Mice
 - GL261 mGBM xenografts
 - GBM xenografts
 - Cells
- METHOD DETAILS
 - Polarization and characterization of Mo-TAM
 - Preparation of cell suspensions from human and mouse glioma tissues
 - scRNA-seq
 - Preprocessing of scRNA-seq data
 - Identification of signature genes for Mo-TAM clusters and myeloid cells

- GSVA
- Hypoxia-associated gene interaction network
- SCENIC analysis
- Cellular interaction analysis
- Cell deconvolution of the human glioma bulk RNA-seq datasets
- GSEA
- Bulk RNA-seq analysis of PBMC-derived Mφ
- Spatial transcriptomic analysis
- Quantitative proteomics analysis
- Metabolomics analysis
- Measurement of SPARC, lactate, and ADM production
- TCM and hypoxia-TAM-CM
- Cell stimulation for p50 nuclear translocation
- Immunofluorescence staining
- Immunohistochemistry staining
- Intravital imaging of mGBM xenograft vasculature
- *In vivo* vascular leakage, tumor hypoxia, and doxorubicin penetration
- *In vitro* vascular permeability imaging assay
- Cell proliferation analysis
- TEM
- MRI imaging
- HPLC analysis
- Immunoblot analysis
- ChIP analysis
- Vector construction and production
- Luciferase reporter assay
- Quantitative real-time PCR (qRT-PCR)
- QUANTIFICATION AND STATISTICAL ANALYSIS
 - Analysis summary
 - Image processing
 - Statistics

SUPPLEMENTAL INFORMATION

Supplemental information can be found online at <https://doi.org/10.1016/j.ccr.2024.03.013>.

ACKNOWLEDGMENTS

We thank Prof. Bo Zhu, Prof. Yan Wang, and Dr. Haofei Liu of Army Medical University for their technical support on the manuscript. This research was supported by grants from the National Key Research and Development Program of China (no. 2021YFA1103000 to Y.S.), the National Natural Science Foundation of China (nos. 82192890, 82192891, and 81821003 to X.-W.B.,

Figure 6. ADM disrupts endothelial adherens junctions via activating CRLR signaling

- (A) Violin plots of cell junction molecule expression in ECs from the WT and *Adm* cKO mGBM xenografts.
- (B) Immunostaining of VE-cadherin in HBMECs treated with rhADM or vehicle. Scale bar, 10 µm.
- (C and D) Immunostaining of VE-cadherin and fluorescein-streptavidin (Strep) (C) and quantification of VE-cadherin⁺ areas and Strep⁺ areas (D) in HBMECs treated with Hypoxia-TAM-CM and/or AMA (*n* = 5 samples/group). Scale bar, 20 µm.
- (E) Inferred interaction of ADM and ADM receptors (CRLR, receptor activity-modifying protein 2 or 3 [RAMP2 or RAMP3]) using CellphoneDB analysis of our hGBM scRNA-seq data.
- (F and G) Immunostaining of CRLR, CD31, and ADM (F) and colocalization rate of CRLR and CD31 (G) in hGBMs (*n* = 5 cases). Scale bar, 20 µm.
- (H and I) Immunostaining of VE-cadherin and Strep (H) and quantification of VE-cadherin⁺ areas and Strep⁺ areas (I) in HBMECs expressing shCRLR or non-targeting shRNA (shNT) in combination with rhADM stimulation (*n* = 5 samples/group). Scale bar, 20 µm.
- (J and K) Immunoblot analyses of Src, VE-cadherin, and their phosphorylated forms in HBMECs with the indicated treatment. Cyto, cytoplasmic; TCL, total cell lysates.
- (L) Schematic illustration of the ADM-CRLR paracrine signal between Hypoxia-TAM and EC. Data are displayed as mean ± SD (A, D, G, and I); two-sided unpaired Wilcoxon test (A); two-way ANOVA (D and I). ns, not significant. **, *p* < 0.01.

See also Figure S7.

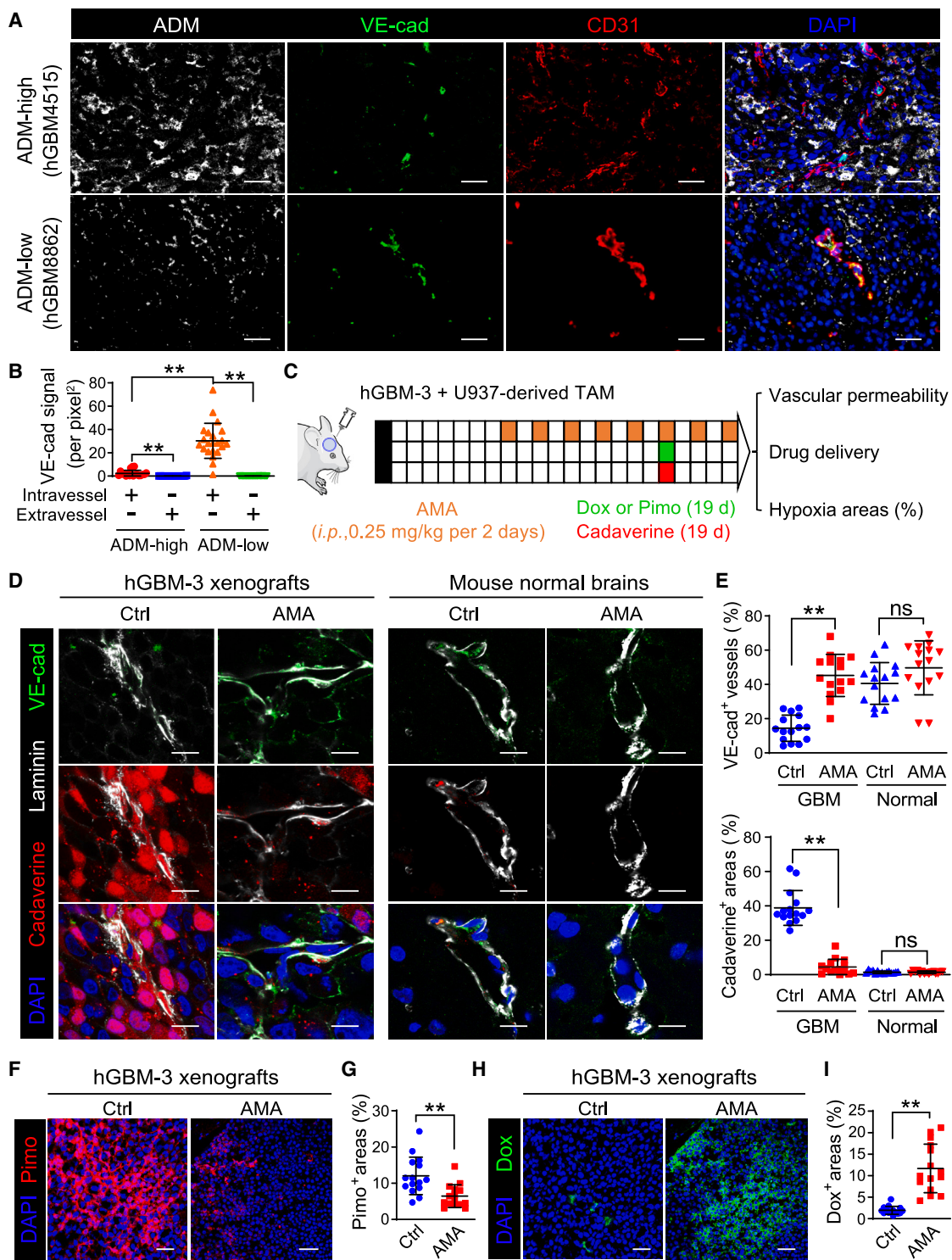


Figure 7. AMA treatment normalizes tumor vasculature in hGBM xenografts

(A) Immunostaining of ADM, VE-cadherin, and CD31 in hGBM tissues. hGBMs ($n = 41$ cases) were stratified based on the proportion of ADM⁺ cells. Scale bar, 50 μ m.

(B) Quantification of VE-cadherin signal in hGBM tissues ($n = 41$ cases, 5 images/case).

(C) Schematic illustration of AMA treatment in mice bearing hGBM-3 xenografts. Cadaverine, doxorubicin (Dox) and pimonidazole (Pimo) were injected intra-venously (*i.p.*).

(D and E) Immunostaining of VE-cadherin, cadaverine and laminin (D), and the percentage of cadaverine effusion areas and VE-cadherin⁺ vessels (E) in hGBM-3 xenografts and mouse normal brains ($n = 15$ images/group). Scale bar, 10 μ m.

(legend continued on next page)

no. 82325041 to Y.-F.P., and nos. 82373191 and 92359303 to Y.S.), and Natural Science Foundation of Chongqing (no. CSTB2023NSCQ-JQX0009 to Y.S., and CSTB2022TIAD-STX0010 to Y.-F.P.).

AUTHOR CONTRIBUTIONS

Y.S. and X.-W.B. developed the hypothesis and designed the experiments. W.W., T.L., Y.C., F.L., and S.Q. performed the experiments and analyzed the data. M.M., J.W., Q.L., Xiaoning Zhang, X. Li, and L.Z. provided clinical specimens and performed clinical analyses. Y.-F.P., H.Q., L.Y., K.Y., Z.H., S.D., Z.Q., Y.Y., X.Y., C.L., Y.G., C.W., Y.L., W.K., J.M., S.Y., M.L., L.A., L.W., L.C., Q.N., and Q.M. provided reagents and technical assistance. X. Liu, Xia Zhang, Z.Z., R.H., and H.F. provided important advice. Y.S. wrote the manuscript. Y.S., X.-W.B., and Y.-F.P. supervised the project.

DECLARATION OF INTERESTS

The authors declare no competing financial interests.

Received: August 1, 2023

Revised: January 21, 2024

Accepted: March 25, 2024

Published: April 18, 2024

REFERENCES

- Horbinski, C., Berger, T., Packer, R.J., and Wen, P.Y. (2022). Clinical implications of the 2021 edition of the WHO classification of central nervous system tumours. *Nat. Rev. Neurol.* **18**, 515–529.
- Hambardzumyan, D., Gutmann, D.H., and Kettenmann, H. (2016). The role of microglia and macrophages in glioma maintenance and progression. *Nat. Neurosci.* **19**, 20–27.
- Cassetta, L., and Pollard, J.W. (2023). A timeline of tumour-associated macrophage biology. *Nat. Rev. Cancer* **23**, 238–257.
- Shi, Y., Ping, Y.F., Zhou, W., He, Z.C., Chen, C., Bian, B.S.J., Zhang, L., Chen, L., Lan, X., Zhang, X.C., et al. (2017). Tumour-associated macrophages secrete pleiotrophin to promote PTPRZ1 signalling in glioblastoma stem cells for tumour growth. *Nat. Commun.* **8**, 15080.
- Su, S., Zhao, J., Xing, Y., Zhang, X., Liu, J., Ouyang, Q., Chen, J., Su, F., Liu, Q., and Song, E. (2018). Immune Checkpoint Inhibition Overcomes ADCP-Induced Immunosuppression by Macrophages. *Cell* **175**, 442–457.e23.
- Kloosterman, D.J., and Akkari, L. (2023). Macrophages at the interface of the co-evolving cancer ecosystem. *Cell* **186**, 1627–1651.
- Ries, C.H., Cannarile, M.A., Hoves, S., Benz, J., Wartha, K., Runza, V., Rey-Giraud, F., Pradel, L.P., Feuerhake, F., Klaman, I., et al. (2014). Targeting Tumor-Associated Macrophages with Anti-CSF-1R Antibody Reveals a Strategy for Cancer Therapy. *Cancer Cell* **25**, 846–859.
- Gholamini, S., Mitra, S.S., Feroze, A.H., Liu, J., Kahn, S.A., Zhang, M., Esparza, R., Richard, C., Ramaswamy, V., Remke, M., et al. (2017). Disrupting the CD47-SIRP α anti-phagocytic axis by a humanized anti-CD47 antibody is an efficacious treatment for malignant pediatric brain tumors. *Sci. Transl. Med.* **9**, eaaf2968.
- Tang, K., Wu, Y.H., Song, Y., and Yu, B. (2021). Indoleamine 2,3-dioxygenase 1 (IDO1) inhibitors in clinical trials for cancer immunotherapy. *J. Hematol. Oncol.* **14**, 68.
- Klichinsky, M., Ruella, M., Shestova, O., Lu, X.M., Best, A., Zeeman, M., Schmierer, M., Gabrusiewicz, K., Anderson, N.R., Petty, N.E., et al. (2020). Human chimeric antigen receptor macrophages for cancer immunotherapy. *Nat. Biotechnol.* **38**, 947–953.
- Cassetta, L., and Pollard, J.W. (2018). Targeting macrophages: therapeutic approaches in cancer. *Nat. Rev. Drug Discov.* **17**, 887–904.
- Cassetta, L., Fragkogianni, S., Sims, A.H., Swierczak, A., Forrester, L.M., Zhang, H., Soong, D.Y.H., Cotechini, T., Anur, P., Lin, E.Y., et al. (2019). Human Tumor-Associated Macrophage and Monocyte Transcriptional Landscapes Reveal Cancer-Specific Reprogramming, Biomarkers, and Therapeutic Targets. *Cancer Cell* **35**, 588–602.e10.
- Klemm, F., Maas, R.R., Bowman, R.L., Kornete, M., Soukup, K., Nassiri, S., Brouland, J.-P., Iacobuzio-Donahue, C.A., Brennan, C., Tabar, V., et al. (2020). Interrogation of the Microenvironmental Landscape in Brain Tumors Reveals Disease-Specific Alterations of Immune Cells. *Cell* **181**, 1643–1660.e17.
- Bowman, R.L., Klemm, F., Akkari, L., Pyonteck, S.M., Sevenich, L., Quail, D.F., Dhara, S., Simpson, K., Gardner, E.E., Iacobuzio-Donahue, C.A., et al. (2016). Macrophage Ontogeny Underlies Differences in Tumor-Specific Education in Brain Malignancies. *Cell Rep.* **17**, 2445–2459.
- Pombo Antunes, A.R., Scheyltjens, I., Lodi, F., Messiaen, J., Antoran, A., Duerinck, J., Kancheva, D., Martens, L., De Vlaeminck, K., Van Hove, H., et al. (2021). Single-cell profiling of myeloid cells in glioblastoma across species and disease stage reveals macrophage competition and specialization. *Nat. Neurosci.* **24**, 595–610.
- Ochocka, N., Segit, P., Walentynowicz, K.A., Wojnicki, K., Cyranowski, S., Swatler, J., Mieczkowski, J., and Kaminska, B. (2021). Single-cell RNA sequencing reveals functional heterogeneity of glioma-associated brain macrophages. *Nat. Commun.* **12**, 1151.
- Yin, W., Ping, Y.F., Li, F., Lv, S.Q., Zhang, X.N., Li, X.G., Guo, Y., Liu, Q., Li, T.R., Yang, L.Q., et al. (2022). A map of the spatial distribution and tumour-associated macrophage states in glioblastoma and grade 4 IDH-mutant astrocytoma. *J. Pathol.* **258**, 121–135.
- Yeo, A.T., Rawal, S., Delcuze, B., Christofides, A., Atayde, A., Strauss, L., Balaj, L., Rogers, V.A., Uhlmann, E.J., Varma, H., et al. (2022). Single-cell RNA sequencing reveals evolution of immune landscape during glioblastoma progression. *Nat. Immunol.* **23**, 971–984.
- Zhang, L., Li, Z., Skrzypczynska, K.M., Fang, Q., Zhang, W., O'Brien, S.A., He, Y., Wang, L., Zhang, Q., Kim, A., et al. (2020). Single-Cell Analyses Inform Mechanisms of Myeloid-Targeted Therapies in Colon Cancer. *Cell* **181**, 442–459.e29.
- Ravi, V.M., Will, P., Kueckelhaus, J., Sun, N., Joseph, K., Salié, H., Vollmer, L., Kuliesiute, U., von Ehr, J., Benotmane, J.K., et al. (2022). Spatially resolved multi-omics deciphers bidirectional tumor-host interdependence in glioblastoma. *Cancer Cell* **40**, 639–655.e13.
- Ren, Y., Huang, Z., Zhou, L., Xiao, P., Song, J., He, P., Xie, C., Zhou, R., Li, M., Dong, X., et al. (2023). Spatial transcriptomics reveals niche-specific enrichment and vulnerabilities of radial glial stem-like cells in malignant gliomas. *Nat. Commun.* **14**, 1028.
- Wang, D., Liu, B., and Zhang, Z. (2023). Accelerating the understanding of cancer biology through the lens of genomics. *Cell* **186**, 1755–1771.
- Qiu, G.Z., Jin, M.Z., Dai, J.X., Sun, W., Feng, J.H., and Jin, W.L. (2017). Reprogramming of the Tumor in the Hypoxic Niche: The Emerging Concept and Associated Therapeutic Strategies. *Trends Pharmacol. Sci.* **38**, 669–686.
- Singleton, D.C., Macann, A., and Wilson, W.R. (2021). Therapeutic targeting of the hypoxic tumour microenvironment. *Nat. Rev. Clin. Oncol.* **18**, 751–772.
- Henze, A.-T., and Mazzone, M. (2016). The impact of hypoxia on tumor-associated macrophages. *J. Clin. Invest.* **126**, 3672–3679.
- Casazza, A., Laoui, D., Wenes, M., Rizzolio, S., Bassani, N., Mambretti, M., Deschoemaeker, S., Van Ginderachter, J.A., Tamagnone, L., and Mazzone, M. (2013). Impeding Macrophage Entry into Hypoxic Tumor

(F and G) Immunostaining of Pimo (F) and the percentage of Pimo $^{+}$ tumor areas (G) in xenografts ($n = 15$ images/group). Scale bar, 50 μ m.

(H and I) Immunostaining of Dox (H) and the percentage of Dox $^{+}$ tumor areas (I) in xenografts ($n = 15$ images/group). Scale bar, 50 μ m.

Data in all quantitative panels are displayed as mean \pm SD; two-way ANOVA (B), and two-tailed unpaired t-test (E, G, and I). ns, not significant. **, $p < 0.01$. See also Figure S8 and Tables S4 and S5.

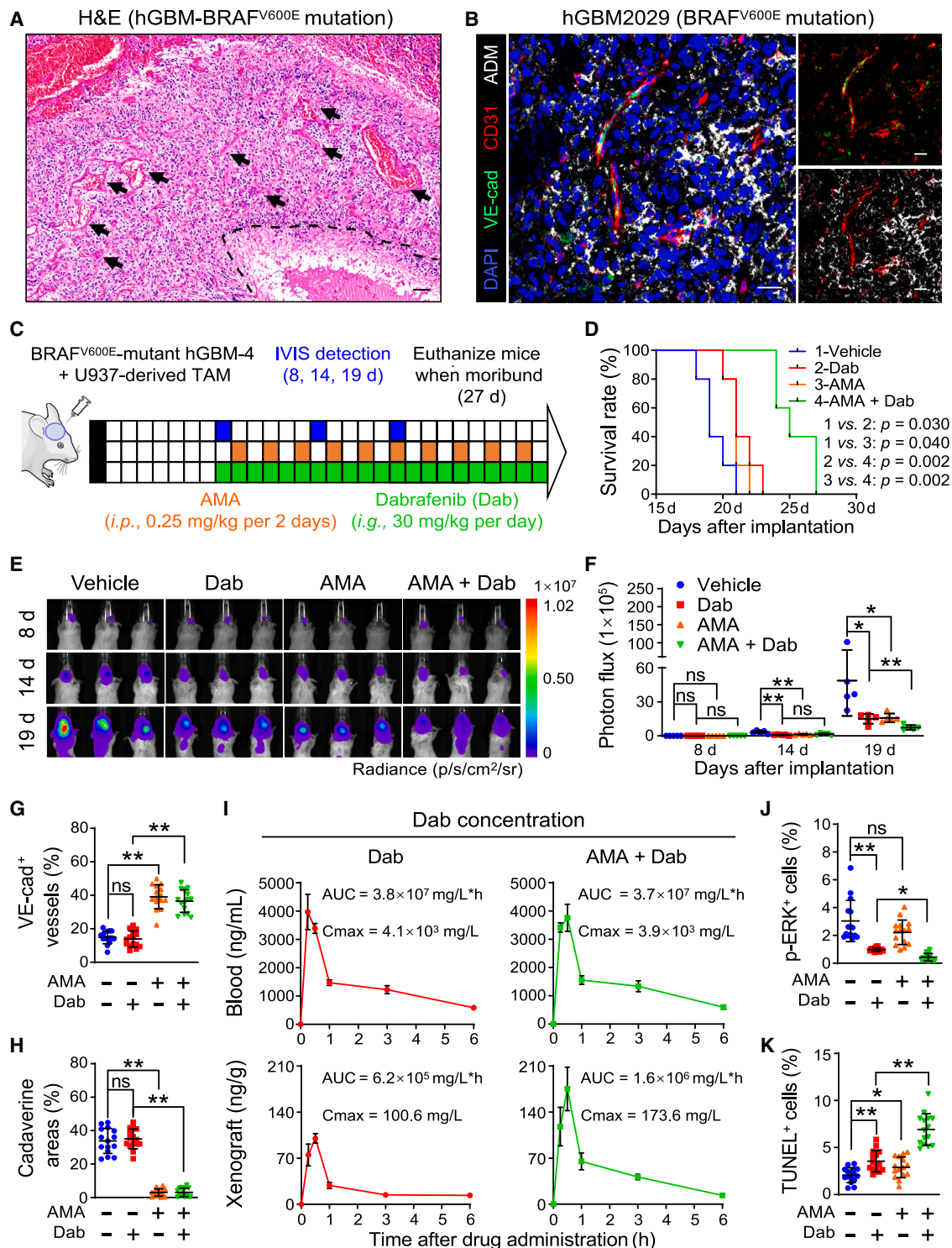


Figure 8. AMA treatment improves dabrafenib delivery and therapeutic efficacy

(A and B) H&E staining (A) and immunostaining of VE-cadherin, CD31, and ADM (B) in BRAF^{V600E}-mutant hGBMs. A necrotic area and vessels at the peri-necrotic area are highlighted by a dashed line and arrows respectively. Scale bar, 100 μm (A) or 25 μm (B).

(C) Schematic of AMA and/or dabrafenib administration. *i.g.*, intragastric injection.

(D) Survival curve of tumor-bearing mice ($n = 5$ mice/group).

(E and F) Bioluminescence images (E) and quantification (F) in xenografts ($n = 5$ mice/group).

(G and H) Percentage of VE-cadherin⁺ vessels (G) and cadaverine effusion areas (H) in xenografts ($n = 15$ images/group).

(legend continued on next page)

- Areas by Sema3A/Nrp1 Signaling Blockade Inhibits Angiogenesis and Restores Antitumor Immunity. *Cancer Cell* 24, 695–709.
27. Bálint, L., Nelson-Maney, N.P., Tian, Y., Serafin, S.D., and Caron, K.M. (2023). Clinical Potential of Adrenomedullin Signaling in the Cardiovascular System. *Circ. Res.* 132, 1185–1202.
 28. Abdelfattah, N., Kumar, P., Wang, C., Leu, J.-S., Flynn, W.F., Gao, R., Baskin, D.S., Pichumani, K., Ijare, O.B., Wood, S.L., et al. (2022). Single-cell analysis of human glioma and immune cells identifies S100A4 as an immunotherapy target. *Nat. Commun.* 13, 767.
 29. Wu, M., Wu, L., Wu, W., Zhu, M., Li, J., Wang, Z., Li, J., Ding, R., Liang, Y., Li, L., et al. (2023). Phagocytosis of Glioma Cells Enhances the Immunosuppressive Phenotype of Bone Marrow-Derived Macrophages. *Cancer Res.* 83, 771–785.
 30. Wu, L., Wu, W., Zhang, J., Zhao, Z., Li, L., Zhu, M., Wu, M., Wu, F., Zhou, F., Du, Y., et al. (2022). Natural Coevolution of Tumor and Immunoenvironment in Glioblastoma. *Cancer Discov.* 12, 2820–2837.
 31. Wu, S.Z., Al-Eryani, G., Roden, D.L., Junankar, S., Harvey, K., Andersson, A., Thennavan, A., Wang, C., Torpy, J.R., Bartonicek, N., et al. (2021). A single-cell and spatially resolved atlas of human breast cancers. *Nat. Genet.* 53, 1334–1347.
 32. Lee, H.-O., Hong, Y., Etioglu, H.E., Cho, Y.B., Pomella, V., Van den Bosch, B., Vanhecke, J., Verbandt, S., Hong, H., Min, J.-W., et al. (2020). Lineage-dependent gene expression programs influence the immune landscape of colorectal cancer. *Nat. Genet.* 52, 594–603.
 33. Bischoff, P., Trinks, A., Obermayer, B., Pett, J.P., Wiederspahn, J., Uhlitz, F., Liang, X., Lehmann, A., Jurmeister, P., Elsner, A., et al. (2021). Single-cell RNA sequencing reveals distinct tumor microenvironmental patterns in lung adenocarcinoma. *Oncogene* 40, 6748–6758.
 34. Ma, L., Hernandez, M.O., Zhao, Y., Mehta, M., Tran, B., Kelly, M., Rae, Z., Hernandez, J.M., Davis, J.L., Martin, S.P., et al. (2019). Tumor Cell Biodiversity Drives Microenvironmental Reprogramming in Liver Cancer. *Cancer Cell* 36, 418–430.e6.
 35. Mei, Y., Wang, X., Zhang, J., Liu, D., He, J., Huang, C., Liao, J., Wang, Y., Feng, Y., Li, H., et al. (2023). Siglec-9 acts as an immune-checkpoint molecule on macrophages in glioblastoma, restricting T-cell priming and immunotherapy response. *Nat. Cancer* 4, 1273–1291.
 36. Chen, Y., Zhang, Y., Yin, Y., Gao, G., Li, S., Jiang, Y., Gu, X., and Luo, J. (2005). SPD—a web-based secreted protein database. *Nucleic Acids Res.* 33, D169–D173.
 37. Dejana, E., and Vestweber, D. (2013). The Role of VE-Cadherin in Vascular Morphogenesis and Permeability Control. *Prog. Mol. Biol. Transl. Sci.* 116, 119–144.
 38. Wallez, Y., Cand, F., Cruzalegui, F., Wernstedt, C., Souchelyntsky, S., Vilgrain, I., and Huber, P. (2007). Src kinase phosphorylates vascular endothelial-cadherin in response to vascular endothelial growth factor: identification of tyrosine 685 as the unique target site. *Oncogene* 26, 1067–1077.
 39. Wessel, F., Winderlich, M., Holm, M., Frye, M., Rivera-Galdos, R., Vockel, M., Linnepe, R., Ipe, U., Stadtmann, A., Zarbock, A., et al. (2014). Leukocyte extravasation and vascular permeability are each controlled in vivo by different tyrosine residues of VE-cadherin. *Nat. Immunol.* 15, 223–230.
 40. Park, J.S., Kim, I.K., Han, S., Park, I., Kim, C., Bae, J., Oh, S.J., Lee, S., Kim, J.H., Woo, D.C., et al. (2016). Normalization of Tumor Vessels by Tie2 Activation and Ang2 Inhibition Enhances Drug Delivery and Produces a Favorable Tumor Microenvironment. *Cancer Cell* 30, 953–967.
 41. Arvanitis, C.D., Ferraro, G.B., and Jain, R.K. (2020). The blood–brain barrier and blood–tumour barrier in brain tumours and metastases. *Nat. Rev. Cancer* 20, 26–41.
 42. Horbinski, C., Nabors, L.B., Portnow, J., Baehring, J., Bhatia, A., Bloch, O., Brem, S., Butowski, N., Cannon, D.M., Chao, S., et al. (2023). NCCN Guidelines® Insights: Central Nervous System Cancers, Version 2.2022. *J. Natl. Compr. Canc. Netw.* 21, 12–20.
 43. Andrews, L.J., Thornton, Z.A., Saincher, S.S., Yao, I.Y., Dawson, S., McGuinness, L.A., Jones, H.E., Jefferies, S., Short, S.C., Cheng, H.Y., et al. (2022). Prevalence of BRAFV600 in glioma and use of BRAF Inhibitors in patients with BRAFV600 mutation-positive glioma: systematic review. *Neuro Oncol.* 24, 528–540.
 44. Sattiraju, A., Kang, S., Giotti, B., Chen, Z., Marallano, V.J., Brusco, C., Ramakrishnan, A., Shen, L., Tsankov, A.M., Hambardzumyan, D., et al. (2023). Hypoxic niches attract and sequester tumor-associated macrophages and cytotoxic T cells and reprogram them for immunosuppression. *Immunity* 56, 1825–1843.e6.
 45. Cheng, S., Li, Z., Gao, R., Xing, B., Gao, Y., Yang, Y., Qin, S., Zhang, L., Ouyang, H., Du, P., et al. (2021). A pan-cancer single-cell transcriptional atlas of tumor infiltrating myeloid cells. *Cell* 184, 792–809.e23.
 46. Gerstner, E.R., Duda, D.G., di Tomaso, E., Ryg, P.A., Loeffler, J.S., Sorensen, A.G., Ivy, P., Jain, R.K., and Batchelor, T.T. (2009). VEGF inhibitors in the treatment of cerebral edema in patients with brain cancer. *Nat. Rev. Clin. Oncol.* 6, 229–236.
 47. Sun, Y., Chen, W., Torphy, R.J., Yao, S., Zhu, G., Lin, R., Lugano, R., Miller, E.N., Fujiwara, Y., Bian, L., et al. (2021). Blockade of the CD93 pathway normalizes tumor vasculature to facilitate drug delivery and immunotherapy. *Sci. Transl. Med.* 13, eabc8922.
 48. Vázquez, R., Riveiro, M.E., Berenguer-Daizé, C., O'Kane, A., Gormley, J., Touzelet, O., Rezai, K., Bekradda, M., and Ouafik, L. (2020). Targeting Adrenomedullin in Oncology: A Feasible Strategy With Potential as Much More Than an Alternative Anti-Angiogenic Therapy. *Front. Oncol.* 10, 589218.
 49. McGinnis, C.S., Murrow, L.M., and Gartner, Z.J. (2019). DoubletFinder: Doublet Detection in Single-Cell RNA Sequencing Data Using Artificial Nearest Neighbors. *Cell Syst.* 8, 329–337.e4.
 50. Bloom, J.D. (2018). Estimating the frequency of multiplets in single-cell RNA sequencing from cell-mixing experiments. *PeerJ* 6, e5578.
 51. Butler, A., Hoffman, P., Smibert, P., Papalexi, E., and Satija, R. (2018). Integrating single-cell transcriptomic data across different conditions, technologies, and species. *Nat. Biotechnol.* 36, 411–420.
 52. Tirosh, I., Izar, B., Prakadan, S.M., Wadsworth, M.H., 2nd, Treacy, D., Trombetta, J.J., Rotem, A., Rodman, C., Lian, C., Murphy, G., et al. (2016). Dissecting the multicellular ecosystem of metastatic melanoma by single-cell RNA-seq. *Science* 352, 189–196.
 53. Korsunsky, I., Millard, N., Fan, J., Slowikowski, K., Zhang, F., Wei, K., Baglaenko, Y., Brenner, M., Loh, P.-r., and Raychaudhuri, S. (2019). Fast, sensitive and accurate integration of single-cell data with Harmony. *Nat. Methods* 16, 1289–1296.
 54. Hänelmann, S., Castelo, R., and Guinney, J. (2013). GSVA: gene set variation analysis for microarray and RNA-Seq data. *BMC Bioinf.* 14, 7.
 55. Szklarczyk, D., Kirsch, R., Koutrouli, M., Nastou, K., Mehryar, F., Hachilif, R., Gable, A.L., Fang, T., Doncheva, N.T., Pysyalo, S., et al. (2023). The STRING database in 2023: protein–protein association networks and functional enrichment analyses for any sequenced genome of interest. *Nucleic Acids Res.* 51, D638–D646.
 56. Sherman, B.T., Hao, M., Qiu, J., Jiao, X., Baseler, M.W., Lane, H.C., Imamichi, T., and Chang, W. (2022). DAVID: a web server for functional

(I) High-performance liquid chromatography (HPLC) analysis of dabrafenib concentration in xenografts and blood plasma from tumor-bearing mice ($n = 5$ mice/group). AUC, area under curve. C_{\max} , maximum concentration.

(J and K) Percentage of p-ERK⁺ cells (J) and TUNEL⁺ apoptotic cells (K) in xenografts ($n = 15$ images/group).

Data are shown as mean \pm SD (F–H, J, and K) or mean \pm SEM (I); Log-rank test (D) or two-way ANOVA (F–H, J, and K). ns, not significant. *, $p < 0.05$. **, $p < 0.01$. See also Tables S4 and S5.

- enrichment analysis and functional annotation of gene lists (2021 update). *Nucleic Acids Res.* 50, W216–W221.
57. Shannon, P., Markiel, A., Ozier, O., Baliga, N.S., Wang, J.T., Ramage, D., Amin, N., Schwikowski, B., and Ideker, T. (2003). Cytoscape: A Software Environment for Integrated Models of Biomolecular Interaction Networks. *Genome Res.* 13, 2498–2504.
 58. Aibar, S., González-Blas, C.B., Moerman, T., Huynh-Thu, V.A., Imrichova, H., Hulselmans, G., Rambow, F., Marine, J.-C., Geurts, P., Aerts, J., et al. (2017). SCENIC: single-cell regulatory network inference and clustering. *Nat. Methods* 14, 1083–1086.
 59. Huynh-Thu, V.A., Irrthum, A., Wehenkel, L., Geurts, P., and Geurts, P. (2010). Inferring Regulatory Networks from Expression Data Using Tree-Based Methods. *PLoS One* 5, e12776.
 60. Efremova, M., Vento-Tormo, M., Teichmann, S.A., and Vento-Tormo, R. (2020). CellPhoneDB: inferring cell–cell communication from combined expression of multi-subunit ligand–receptor complexes. *Nat. Protoc.* 15, 1484–1506.
 61. Jew, B., Alvarez, M., Rahmani, E., Miao, Z., Ko, A., Garske, K.M., Sul, J.H., Pietiläinen, K.H., Pajukanta, P., and Halperin, E. (2020). Accurate estimation of cell composition in bulk expression through robust integration of single-cell information. *Nat. Commun.* 11, 1971.
 62. Dobin, A., Davis, C.A., Schlesinger, F., Drenkow, J., Zaleski, C., Jha, S., Batut, P., Chaisson, M., and Gingeras, T.R. (2013). STAR: ultrafast universal RNA-seq aligner. *Bioinformatics* 29, 15–21.
 63. Liao, Y., Smyth, G.K., and Shi, W. (2014). featureCounts: an efficient general purpose program for assigning sequence reads to genomic features. *Bioinformatics* 30, 923–930.
 64. Love, M.I., Huber, W., and Anders, S. (2014). Moderated estimation of fold change and dispersion for RNA-seq data with DESeq2. *Genome Biol.* 15, 550.
 65. Wu, T., Hu, E., Xu, S., Chen, M., Guo, P., Dai, Z., Feng, T., Zhou, L., Tang, W., Zhan, L., et al. (2021). clusterProfiler 4.0: A universal enrichment tool for interpreting omics data. *Innovation* 2, 100141.
 66. Ginestet, C. (2011). ggplot2: Elegant Graphics for Data Analysis. *J. R. Stat. Soc. Ser. A Stat. Soc.* 174, 245–246.
 67. Kleshchevnikov, V., Shmatko, A., Dann, E., Avazidis, A., King, H.W., Li, T., Elmentait, R., Lomakin, A., Kedlian, V., Gayoso, A., et al. (2022). Cell2location maps fine-grained cell types in spatial transcriptomics. *Nat. Biotechnol.* 40, 661–671.
 68. Puchalski, R.B., Shah, N., Miller, J., Dalley, R., Nomura, S.R., Yoon, J.-G., Smith, K.A., Lanknerovich, M., Bertagnoli, D., Bickley, K., et al. (2018). An anatomic transcriptional atlas of human glioblastoma. *Science* 360, 660–663.
 69. Bankhead, P., Loughrey, M.B., Fernández, J.A., Dombrowski, Y., McArt, D.G., Dunne, P.D., McQuaid, S., Gray, R.T., Murray, L.J., Coleman, H.G., et al. (2017). QuPath: Open source software for digital pathology image analysis. *Sci. Rep.* 7, 16878.
 70. Gu, Z., Eils, R., and Schlesner, M. (2016). Complex heatmaps reveal patterns and correlations in multidimensional genomic data. *Bioinformatics* 32, 2847–2849.
 71. Tyanova, S., Temu, T., and Cox, J. (2016). The MaxQuant computational platform for mass spectrometry-based shotgun proteomics. *Nat. Protoc.* 11, 2301–2319.
 72. UniProt Consortium (2021). UniProt: the universal protein knowledgebase in 2021. *Nucleic Acids Res.* 49, D480–D489.
 73. Xie, G., Wang, L., Chen, T., Zhou, K., Zhang, Z., Li, J., Sun, B., Guo, Y., Wang, X., Wang, Y., et al. (2021). A Metabolite Array Technology for Precision Medicine. *Anal. Chem.* 93, 5709–5717.
 74. Shi, Y., Guryanova, O.A., Zhou, W., Liu, C., Huang, Z., Fang, X., Wang, X., Chen, C., Wu, Q., He, Z., et al. (2018). Ibrutinib inactivates BMX-STAT3 in glioma stem cells to impair malignant growth and radioresistance. *Sci. Transl. Med.* 10, eaah6816.
 75. Zhou, W., Chen, C., Shi, Y., Wu, Q., Gimple, R.C., Fang, X., Huang, Z., Zhai, K., Ke, S.Q., Ping, Y.F., et al. (2017). Targeting Glioma Stem Cell-Derived Pericytes Disrupts the Blood-Tumor Barrier and Improves Chemotherapeutic Efficacy. *Cell Stem Cell* 21, 591–603.e4.

STAR★METHODS

KEY RESOURCES TABLE

REAGENT or RESOURCE	SOURCE	IDENTIFIER
Antibodies		
anti-human Adrenomedullin /ADM (polyclonal)	Abcam	cat# ab69117, RRID: AB_1565816
anti-mouse Adrenomedullin /ADM (polyclonal)	Abcam	cat# ab190819, RRID: AB_3083423
anti-human CD11b-C-terminal (Clone EP1345Y)	Abcam	cat# ab52478, RRID: AB_868788
anti-mouse CD11b (Clone M1/70)	Thermo Fisher Scientific	cat# 14-0112-82, RRID: AB_467108
anti-human CD31 (PECAM-1) (Clone 89C2)	Cell Signaling Technology	cat# 3528, RRID: AB_2160882
anti-mouse CD31 (Clone MEC 7.46)	Abcam	cat# ab7388, RRID: AB_305905
anti-human Laminin alpha 4/LAMA4 (polyclonal)	Abcam	cat# ab209675, RRID: AB_3094532
anti-mouse/human VE-cadherin- Intercellular Junction Marker (polyclonal)	Abcam	cat# ab33168, RRID: AB_870662
anti-human CRLR (polyclonal)	Abcam	cat# ab84467, RRID: AB_10672189
anti-mouse/human CD140b (PDGFRB) (Clone APB5)	Thermo Fisher Scientific	cat# 14-1402-82, RRID: AB_467493
anti-mouse/human Claudin-5 (Clone 4C3C2)	Thermo Fisher Scientific	cat# 35-2500, RRID: AB_2533200
anti-mouse/human Galectin-3 (Mac-2) (Clone Gal397)	Biolegend	cat# 126702, RRID: AB_1134256
anti-mouse/human Iba1 (polyclonal)	FUJIFILM Wako	cat# 019-19741, RRID: AB_839504
anti-human NF-κB1 p105/p50 (polyclonal)	Cell Signaling Technology	cat# 3035, RRID: AB_330564
anti-mouse/human Normal Rabbit IgG	Cell Signaling Technology	cat# 2729, RRID: AB_1031062
anti-mouse/human Phospho-p44/42 MAPK (Erk1/2) (Thr202/Tyr204) (Clone D13.14.4E)	Cell Signaling Technology	cat# 4370, RRID: AB_2315112
anti-human BRAF (V600E) (Clone RM8)	Merck	cat# SAB5600047, RRID: AB_3083425
anti-human VE Cadherin (phospho Y685) (polyclonal)	Abcam	cat# ab119785, RRID: AB_10971838
anti-mouse/human SRC Family (phospho Y418) (Clone EP503Y)	Abcam	cat# ab40660, RRID: AB_776106
anti-mouse/human Src (polyclonal)	Cell Signaling Technology	cat# 2108, RRID: AB_331137
anti-mouse/human GAPDH (Clone D16H11)	Cell Signaling Technology	cat# 5174, RRID: AB_10622025
Biological samples		
Primary tumor samples	the Biobank of Southwest Hospital	N/A
Chemicals, peptides, and recombinants proteins		
Adrenomedullin (22-52) Peptide (AMA)	Bioss	cat# Y-0184
Dabrafenib (GSK2118436)	Selleckchem	cat# S2807
Neurobasal™-A Medium, minus phenol red	Thermo Fisher Scientific	cat# 12349015
B-27™ Supplement (50X), serum free	Thermo Fisher Scientific	cat# 17504-044
Human EGF, Animal-Free Recombinant Protein	Thermo Fisher Scientific	cat# AF-100-15
Human FGF-basic (FGF-2/bFGF) (154 aa), Animal-Free Recombinant Protein	Thermo Fisher Scientific	cat# AF-100-18B
MEM Non-Essential Amino Acids Solution (100X)	Thermo Fisher Scientific	cat# 11140050
GlutaMAX™ Supplement	Thermo Fisher Scientific	cat# 35050061
Sodium Pyruvate (100 mM)	Thermo Fisher Scientific	cat# 11360070
Endothelial cell medium	ScienCell Research Laboratory	cat# 1001
RPMI 1640 Medium	Thermo Fisher Scientific	cat# 11875093
Fetal Bovine Serum	Thermo Fisher Scientific	cat# 10099141
Penicillin-Streptomycin 100X solution	HyClone	cat# SV30010

(Continued on next page)

Continued

REAGENT or RESOURCE	SOURCE	IDENTIFIER
CD14 MicroBeads, human	Miltenyi Biotec	cat# 130-050-201
Human M-CSF Recombinant Protein	Thermo Fisher Scientific	cat# 300-25
Mouse M-CSF Recombinant Protein	Thermo Fisher Scientific	cat# 315-02
Normal Donkey Serum	Solarbio	cat# SL050
TritonX-100	Solarbio	cat# T8200
Dextran, Tetramethylrhodamine, 70,000 MW, Neutral	Thermo Fisher Scientific	cat# D1819
Alexa Fluor™ 647 Cadaverine	Thermo Fisher Scientific	cat# A30679
Doxorubicin hydrochloride	Merck	cat# D1515
RNAiso Plus	Takara Biotechnology	cat# 9108
Adrenomedullin 52 human	Merck	cat# A2327
PP2	Selleckchem	cat# S7008
RIPA Lysis and Extraction Buffer	Thermo Fisher Scientific	cat# 89900
4',6-diamidino-2-phenylindole	Beyotime	cat# P0131
Antifade Mounting Medium with DAPI		
Fluoromount G	Southern Biotech	cat# 0100-01
Recombinant Human SPARC Protein, CF	R&D Systems	cat# 941-SP-050
Sodium L-lactate	Merck	cat# L7022
Resatorvid (TAK-242)	Selleckchem	cat# S7455
Sodium oxamate (SO)	Selleckchem	cat# S6871
VivoGlo™ Luciferin, <i>In Vivo</i> Grade	Promega	cat# P1043
Godoteric acid	Guerbet	N/A
Critical commercial assays		
Brain Tumor Dissociation Kit	Miltenyi Biotec	cat# 130-095-942
GemCode Single Cell 3' Gel Bead and Library Kit	10x Genomics	cat# 1000002
Chromium i7 Multiplex Kit	10x Genomics	cat# 120262
One Step TUNEL Apoptosis Assay Kit	Beyotime	cat# C1090
Opal Polaris 7 Color IHC Detection Kits	AKOYA	cat# NEL871001KT
Cell Counting Kit-8	Beyotime	cat# C0038
SimpleChIP Plus Enzymatic Chromatin IP Kit (Magnetic Beads)	Cell Signaling Technology	cat# 9005
Dual-Glo® Luciferase Assay System	Promega	cat# E2920
Pierce™ Quantitative Colorimetric Peptide Assay kit	Thermo Fisher Scientific	cat# 23275
Tandem Mass Tags (TMT) 10-plex reagents	Thermo Fisher Scientific	cat# 90110
Human SPARC Quantikine ELISA Kit	R&D Systems	cat# DSP00
Human Adrenomedullin ELISA kit	Phoenix Pharmaceuticals	cat# EK-010-01
L-Lactate Assay Kit	Abcam	cat# ab65331
Eponate 12™ Kit with DMP-30	TED PELLA	cat# 18010
Pimonidazole hydrochloride	Hypoxyprobe	cat# HP1-100
Dako REAL EnVision Detection System	Agilent	cat# K500711-2
<i>In Vitro</i> Vascular Permeability Imaging Assay	MERCK	cat# 17-10398
Deposited data		
Human glioma scRNA-seq data	this paper	National Genomics Data Center of China, PRJCA008116, OMIX002713
Human PBMC-derived Mφ bulk RNA-seq	this paper	National Genomics Data Center of China, PRJCA008116, OMIX005630

(Continued on next page)

Continued

REAGENT or RESOURCE	SOURCE	IDENTIFIER
Mouse GBM scRNA-seq data	this paper	National Genomics Data Center of China, PRJCA008116, OMIX004529
Mouse GBM scRNA-seq data	Ochocka et al., 2021 ¹⁶	GEO database: GSE136001
Mouse GBM scRNA-seq data	Yeo et al., 2022 ¹⁸	GEO database: GSE196175
Human GBM scRNA-seq data	Abdelfattah et al., 2022 ²⁸	GEO database: GSE182109
Human GBM scRNA-seq data	Wu et al., 2022 ³⁰	Genome Sequence Archive, HRA002913
Human breast adenocarcinoma scRNA-seq data	Wu et al., 2022 ³¹	GEO database: GSE176078
Human colorectal adenocarcinoma scRNA-seq data	Lee et al., 2020 ³²	GEO database: GSE132465
Human lung adenocarcinoma scRNA-seq data	Bischoff et al., 2021 ³³	https://doi.org/10.24433/CO.0121060.v1
Human hepatic cell carcinoma scRNA-seq data	Ma et al., 2021 ³⁴	GEO database: GSE151530
Human glioma bulk RNA-seq data	TCGA database	https://portal.gdc.cancer.gov/
Human glioma bulk RNA-seq data	Ivy GBM Atlas Project	http://glioblastoma.alleninstitute.org/
Human GBM spatial transcriptomics data	Ravi et al., 2022 ²⁰	Dryad database https://datadryad.org/stash/dataset/doi:10.5061/dryad.h70rxwdmj
Human GBM spatial transcriptomics data	Ren et al., 2023 ²¹	GEO database, GSE194329
Human GBM spatial transcriptomics data	Mei et al., 2023 ³⁵	National Genomics Data Center of China, PRJCA015974, OMIX003593
Experimental models: cell lines		
GL261	Institute of Transfusion Medicine	N/A
GL261-luciferase	Institute of Transfusion Medicine	N/A
hGBM-3	this paper	N/A
hGBM-3-luciferase	this paper	N/A
hGBM-4	this paper	N/A
hGBM-4-luciferase	this paper	N/A
Human brain microvascular endothelial cell (HBMEC)	ScienCell Research Laboratory	cat# 1000
U937	ATCC	cat# CRL-1593.2, RRID: CVCL_0007
Experimental models: Organisms/strains		
C57BL/6 <i>Ccr2-Cre-eGFP</i>	Biocytogen Pharmaceuticals	N/A
C57BL/6 <i>Adm</i> ^{f/f}	Biocytogen Pharmaceuticals	N/A
NOD-SCID mice	Hunan SJA Laboratory Animal Co., Ltd.	N/A
Oligonucleotides		
shRNA sequences, see Table S6	this paper	N/A
qRT-PCR primers, see Table S7	this paper	N/A
Software and algorithms		
<i>In Vivo</i> Animal Imaging System	Biolight Biotechnology	https://www.blt-imaging.com/
ImageJ bundled with 64-bit Java 8	National Institutes of Health	https://imagej.nih.gov/ij/ RRID: SCR_003070
StrataQuest software version 7.1.119	Tissue Gnostics GmbH	https://www.tissuegnostics.cn/strataquest/ RRID: SCR_024861
AngioTool version 0.5	National Institutes of Health	https://angiotool.software.informer.com/ RRID: SCR_016393
Avizo version 2019.1	Thermo Fisher Scientific	https://www.thermofisher.cn/ RRID: SCR_014431
Imaris version 9.0.1	Oxford Instruments	https://imaris.oxinst.com/ RRID: SCR_007370

(Continued on next page)

Continued

REAGENT or RESOURCE	SOURCE	IDENTIFIER
GraphPad Prism 9	GraphPad	https://www.graphpad.com/ RRID: SCR_002798
R software version 3.6.3	The R Foundation	https://cran.r-project.org/ RRID: SCR_003005
Python version 3.7.4	Python Software Foundation	https://www.python.org RRID: SCR_008394
MassLynx version 4.1	Waters	https://www.waters.com/waters/zh_CN/MassLynx-Mass-Spectrometry-Software-/ RRID: SCR_014271
ZEN version 3.6	ZEISS	https://www.zeiss.com/microscopy/en/products/software/zeiss-zen.html RRID: SCR_013672
Bruker Pharmascan 7T	Bruker	https://www.bruker.com/zh.html RRID: SCR_012326
Omni-kinetics workstation version 2.0	GE Healthcare	N/A
MSigDB version 7.5.1	GSEA and MSigDB Team	https://CRAN.R-project.org/package=msigdb RRID: SCR_022870
DoubletFinder version 2.0.3	McGinnis et al., 2019 ⁴⁹	https://github.com/chris-mcginnis-ucsf/DoubletFinder RRID: SCR_018771
Seurat pipeline version 4.0.3	Butler et al., 2018 ⁵¹	https://satijalab.org/seurat/index.html RRID: SCR_016341
inferCNV version 1.10.1	Tirosh et al., 2016 ⁵²	https://www.bioconductor.org/packages/release/bioc/html/infercnv.html RRID: SCR_021140
Harmony version 0.1.0	Korsunsky et al., 2019 ⁵³	https://github.com/immunogenomics/harmony RRID: SCR_022206
GSVA version 1.48.3	Hänelmann et al., 2013 ⁵⁴	https://bioconductor.org/packages/release/bioc/html/GSVA.html RRID: SCR_021058
STRING	Szklarczyk et al., 2022 ⁵⁵	https://string-db.org/ RRID: SCR_005223
DAVID	Sherman et al., 2022 ⁵⁶	https://david.ncifcrf.gov/ RRID: SCR_001881
Cytoscape version 3.10.0	Shannon et al., 2003 ⁵⁷	https://cytoscape.org/ RRID: SCR_003032
Scenic version 1.2.4	Aibar et al., 2017 ⁵⁸	https://github.com/aertslab/SCENIC RRID: SCR_017247
GENIE3 version 1.22.0	Aibar et al., 2017 ⁵⁸	https://bioconductor.org/packages/release/bioc/html/GENIE3.html RRID: SCR_000217
AUcell version 1.2.4	Aibar et al., 2017 ⁵⁸	https://bioconductor.org/packages/release/bioc/html/AUCell.html RRID: SCR_021327
RcisTarget version 1.20.0	Isalan et al., 2010 ⁵⁹	https://bioconductor.org/packages/release/bioc/html/RcisTarget.html RRID: SCR_024860
CellphoneDB version 2.0	Efremova et al. 2020 ⁶⁰	https://www.cellphonedb.org/ RRID: SCR_017054
BisqueRNA version 1.0.5	Jew et al., 2020 ⁶¹	https://github.com/cran/BisqueRNA RRID: SCR_005564
STAR aligner version 2.7.1	Dobin et al., 2013 ⁶²	https://github.com/alexdobin/STAR RRID: SCR_004463

(Continued on next page)

Continued

REAGENT or RESOURCE	SOURCE	IDENTIFIER
featureCounts version 2.0.3	Liao et al., 2014 ⁶³	https://github.com/topics/featurecounts RRID: SCR_012919
DESeq2 version 1.40.2	Love et al., 2014 ⁶⁴	https://github.com/thelovelab/DESeq2 RRID: SCR_015687
clusterProfiler version 4.8.1	Wu et al., 2021 ⁶⁵	https://github.com/YuLab-SMU/clusterProfiler RRID: SCR_016884
FactoMineR version 2.8	FactoMineR team	https://cran.r-project.org/web/packages/FactoMineR/
ggplot2 version 3.4.2	Ginestet, 2011 ⁶⁶	https://github.com/tidyverse/ggplot2 RRID: SCR_014601
cell2location version 0.9.0	Kleshchevnikov et al., 2022 ⁶⁷	https://github.com/BayraktarLab/cell2location RRID: SCR_024859
Qupath version 0.4.3	Bankhead et al., 2017 ⁶⁸	https://qupath.github.io/ RRID: SCR_018257
ComplexHeatmap version 2.16.0	Gu et al., 2016 ⁷⁰	https://bioconductor.org/packages/release/bioc/html/ComplexHeatmap.html RRID: SCR_017270
Maxquant version 1.6.15.0	Tyanova et al., 2017 ⁷¹	https://www.maxquant.org/ RRID: SCR_014485
Uniprot	Consortium 2020 ⁷²	https://www.uniprot.org/ RRID: SCR_002380
SpaceRanger version 1.3.0	10xGenomics	https://www.10xgenomics.com/support/software/space-ranger/ RRID: SCR_023571

RESOURCE AVAILABILITY

Lead contact

Requests for further information should be directed to Yu Shi (shiyu@tmmu.edu.cn).

Materials availability

Requests for resources and reagents should be directed to and will be fulfilled by the **lead contact**, Yu Shi (shiyu@tmmu.edu.cn).

Data and code availability

- scRNA-seq and bulk RNA-seq data have been deposited at the National Genomics Data Center of China (<https://ngdc.cncb.ac.cn/>) under accession number PRJCA008116 (human scRNA-seq: OMIX002713, mouse scRNA-seq: OMIX004529; human bulk RNA-seq: OMIX005630), and are publicly available as of the date of publication.
- The accession numbers for public scRNA-seq datasets, bulk RNA-seq datasets and spatial transcriptomics datasets are listed in the [key resources table](#). The code supporting the current study is available from the **lead contact** upon reasonable request.
- Any additional information required to reanalyze the data reported in this paper is available from the **lead contact** upon reasonable request.

EXPERIMENTAL MODEL AND SUBJECT DETAILS

hGBM specimens

Surgical hGBM specimens were obtained from the Biobank of Southwest Hospital, with approval from the Ethics Committee of Southwest Hospital and informed consent from patients or their guardians. The clinicopathological information is summarized in **Tables S1** and **S4**. Thirty-one fresh specimens were subjected to scRNA-seq and two fresh specimens were used for cell culture. Forty-five formalin-fixed and paraffin-embedded specimens were used for immunostaining. All procedures were performed in accordance with the principles of the Declaration of Helsinki.

EXPERIMENTAL MOUSE MODELS

Mice

C57BL/6 *Ccr2*-Cre-eGFP or *Adm*^{f/f} transgenic mice (Biocytogen Pharmaceuticals) were generated by inserting Cre-eGFP into exon 3 of *Ccr2* or loxP into flanking exon 1 to 3'UTR of *Adm* in mouse embryonic stem cells. Female non-obese diabetic/severe combined immunodeficiency (NOD-SCID) mice aged 4–6 weeks were purchased from Hunan SJA Laboratory Animal. Mice were kept in ventilated cages under specific pathogen-free conditions, maintained in a 12-h light/12-h dark cycle at 20–24°C, and provided sterilized water and food at the Laboratory Animal Center of Southwest Hospital. All animal experiments were performed in accordance with the protocols approved by the Animal Experimentation Ethics Committee of Army Medical University.

GL261 mGBM xenografts

The GL261 cell line was a kind gift from Prof. Zi-ling Wang (Beijing Institute of Transfusion Medicine). GL261 (n = 25,000 cells) expressing the luciferase reporter were implanted into the right frontal lobe of C57BL/6 *Ccr2*-Cre-eGFP or *Adm* cKO mice as previously described.⁴ Mice were sacrificed at the indicated time points after tumor implantation or upon the manifestation of neurological symptoms. Xenografts were harvested to evaluate histological or molecular features.

GBM xenografts

hGBM cells (hGBM-3, -4; n = 2,000) expressing luciferase reporter were implanted alone or co-implanted with U937-derived TAMs (n = 20,000) into the right frontal lobe of NOD-SCID mice to establish intracranial xenografts as previously described.⁴ Since day nine after implantation of tumor cells, mice bearing hGBM-3 xenografts were intraperitoneally injected with 0.25 mg/kg AMA (Bioss) or phosphate-buffered saline (PBS) vehicle every other day. Mice bearing hGBM-4 xenografts were administrated with AMA, 30 mg/kg dabrafenib (Selleckchem) daily through intragastric injection, their combination, or vehicle. Tumor growth was monitored by bioluminescence imaging using *In Vivo* Animal Imaging System (BioLight Biotechnology). Mice were sacrificed at the indicated time points or upon the manifestation of neurological symptoms, and xenografts were harvested for further analyses.

Cells

The hGBM cells dissociated from surgical hGBM tissues were routinely maintained as xenografts in immunodeficient mice or cultured in Neurobasal-A medium supplemented with B27, 10 ng/ml epidermal growth factor, 10 ng/ml basic fibroblast growth factor, 1× MEM non-essential amino acids, 1× GlutaMAX, and 1× sodium pyruvate (Thermo Fisher Scientific) as previously described.⁴ Clinical information of hGBM-3 and hGBM-4 cells is summarized in Table S5. CD14⁺ monocytes were isolated from PBMCs of healthy donors using anti-CD14 microbeads (Miltenyi Biotec) using magnetic activated cell sorting. Human monocyte line U937 (ATCC) was maintained in RPMI-1640 medium supplemented with 10% fetal bovine serum (FBS, Thermo Fisher Scientific). HBMECs (ScienCell) were cultured in EC medium (ScienCell). Cells were cultured in a humidified incubator at 37°C with 5% CO₂ and atmospheric O₂ unless otherwise indicated. Penicillin-streptomycin solution (HyClone) was used to prevent contamination.

METHOD DETAILS

Polarization and characterization of Mo-TAM

Human CD14⁺ monocytes from healthy donors, U937 cells, and mouse BMDMs were used for Mo-TAM polarization as previously described.^{4,5} PBMC-derived CD14⁺ monocytes and U937 cells were maintained in RPMI 1640 medium supplemented with 20 ng/ml macrophage colony-stimulating factor (M-CSF) (Thermo Fisher Scientific) and 10% FBS for four days and then cocultured with hGBM-3 cells using 0.4 µm transwell chamber or treated with TCM for four additional days for TAM polarization. The Hypoxia-TAM signature was induced by culturing these TAMs under 1% O₂ for two days. For polarization of mouse BMDM, bone marrow cells were harvested from the femurs and the tibias of C57BL/6 mice and were cultured in RPMI 1640 medium with 10% FBS and 100 ng/mL M-CSF (Thermo Fisher Scientific) for four days. BMDM-derived TAMs were induced by maintaining BMDM in GL261 TCM for four additional days.

Preparation of cell suspensions from human and mouse glioma tissues

Fresh human tumor tissues were placed on ice and transported to the laboratory within 2 h after tumor resection, followed by tumor dissection and processing. The samples were thoroughly washed with precooled PBS on ice to remove visible blood clots. Subsequently, the tumor tissues were mechanically minced into small pieces and further dissociated into single-cell suspensions using a brain tumor dissociation kit (Miltenyi Biotec) following the manufacturer's instructions. The homogenate was filtered through a 40 µm strainer and centrifuged at 300 × g for 10 min at 4°C. After washing the homogenate with PBS containing 2% FBS, cell number was counted, and the suspension was diluted to an appropriate concentration for library construction and sequencing. Mouse tumor tissues were minced into pieces and incubated with a brain tumor dissociation kit (Miltenyi Biotec) for 30 min at 37°C. Subsequently, the homogenate was filtered through a 70 µm strainer and centrifuged at 500 × g for 5 min at 4°C. The cell suspension underwent a similar procedure as described above.

scRNA-seq

scRNA-seq was performed on the 10x Genomics platform, and libraries were generated using a GemCode Single-Cell 3' Gel Bead and Library Kit and a Chromium i7 Multiplex Kit (10x Genomics) according to the manufacturer's instructions. Briefly, 10,000–20,000 live cells were loaded onto a GemCode Single-Cell Instrument to generate single-cell gel beads-in-emulsions (GEMs). After reverse transcription, the GEMs were disrupted, and barcoded complementary DNA was isolated and amplified using polymerase chain reaction (PCR). Following enzymatic fragmentation, end repair, A-tailing, adapter ligation, and index-PCR, sample indices were determined using a 2100 BioAnalyzer (Agilent Technologies). Purified libraries were sequenced using a NovaSeq 6000 system (Illumina).

Preprocessing of scRNA-seq data

Potential doublets were identified using DoubletFinder (v.2.0.3)⁴⁹ at a threshold of 0.075 and filtered out.⁵⁰ The Seurat pipeline (v.4.0.3) was applied to each sample for integrated analyses.⁵¹ Genes expressed in < 5 cells and cells expressing < 300 or > 7,000 genes (outliers) or having mitochondrial genes > 20% were excluded. We inferred CNVs using the inferCNV⁵² method and classified cells as malignant or non-malignant. Subsequently, a harmony algorithm⁵³ was employed to mitigate batch effects across the samples. Principal component analysis (PCA) was performed on the 2,000 top highly variable genes using the RunPCA function in Seurat. UMAP dimensional reduction was performed on the scaled matrix using the first 20 principal components to obtain a two-dimensional representation. We used the FindClusters function in Seurat to identify clusters on the first 20 principal components with a resolution of 0.4.

Identification of signature genes for Mo-TAM clusters and myeloid cells

The FindAllMarkers function in Seurat was used to identify Mo-TAM cluster-specific alterations (upregulated genes in a certain Mo-TAM cluster versus other Mo-TAM clusters) and myeloid-specific alterations (upregulated genes in myeloid cells versus other cell types) using our hGBM scRNA-seq dataset. Cluster-specific alterations were identified using the following selection criteria: fold change ≥ 1.5 and adjusted $p < 0.05$. Myeloid-specific alterations were identified using the following selection criteria: pct.1-pct.2 ≥ 0.3 , fold change ≥ 2 , adjusted $p < 0.05$, and expression observed in $\geq 50\%$ of the total cells within a certain cell type. A core gene signature of each Mo-TAM cluster was extracted by intersecting cluster-specific alterations with myeloid-specific alterations for cell deconvolution analysis.

GSVA

We retrieved the human C2 and C5 genesets from the MSigDB using the msigdb R package (v.7.5.1). The GetAssaydata function in Seurat was employed to extract the single-cell count matrix. GSVA (v.1.48.3)⁵⁴ was utilized to perform GSVA analysis on the single-cell count matrix with parameters set as "kcdf = Gaussian" and "method = zscore". Z-scores were computed for each cell and the single-cell z-score matrix was written into a newly created matrix within the Seurat object. The FindAllMarkers function in Seurat was used to identify core pathways for each cluster, with threshold criteria set as adjusted $p < 0.05$ and Log2 fold change ≥ 1 .

Hypoxia-associated gene interaction network

The core HRGs in the Hypoxia-TAM cluster were defined as the intersections of the upregulated genes of Hypoxia-TAM (adjusted $p < 0.05$, Log2 fold change ≥ 0.5) and those in a hypoxia geneset (HARRIS_HYPOXIA, MSigDB). Hypoxia scoring for each cell within the Hypoxia-TAM cluster was performed using the AddModuleScore function in Seurat. To screen for the uncovered hypoxia-associated genes in the Hypoxia-TAM cluster, we analyzed the correlation between the expression of a certain gene and the corresponding hypoxia score in each Hypoxia-TAM cell using Pearson correlation analysis. The 100 top genes with the most significant positive or negative correlation were retained. These candidates were overlapped with the differentially expressed genes (DEGs) in the Hypoxia-TAM cluster relative to those in other Mo-TAM clusters in the scRNA-seq data (adjusted $p < 0.05$, Log2 fold change ≥ 0.5) to identify HPGs and HNGs. The interactions among the core HRGs and HPGs or HNGs in Hypoxia-TAM were predicted using the STRING database⁵⁵ (interaction types = "Experiments," "Databases," and "Co-expression"). The DAVID database⁵⁶ was used for clustering (clustering strength = "median") of HPGs and HNGs, followed by functional annotations. The gene interaction network was visualized using Cytoscape (v.3.10.0).⁵⁷

SCENIC analysis

SCENIC algorithm⁵⁸ was employed to infer different regulons (TFs and their target genes) across Mo-TAM clusters. Briefly, a subset of 1,000 Mo-TAMs was extracted from the scRNA-seq data of hGBM-IDHwt-7 and hGBM-IDHwt-17 that showed apparent necrotic areas. We employed GENIE3 (v.1.22.0)⁵⁸ to identify the co-expression modules between TFs and potential target genes using the gene-expression matrix. Subsequently, cis-regulatory motif enrichment analysis for each co-expression module among all potential target genes was performed using RcisTarget (v.1.20.0).⁵⁹ Only target genes with enriched motifs corresponding to the TFs were selected as direct targets, and 282 regulons were identified. The activity of each regulon in each cell was scored using AUCell (v.1.2.4).⁵⁸

Cellular interaction analysis

Intercellular interactions were investigated across ECs and Mo-TAM clusters in our hGBM scRNA-seq dataset using CellPhoneDB (v.2.0).⁶⁰ The average expression of ligands and receptors in each cell type or cluster was generated and presented as a null distribution for each ligand-receptor pair. The likelihood of cell specificity for a given receptor-ligand complex was calculated.

Cell deconvolution of the human glioma bulk RNA-seq datasets

BisqueRNA (Bisque, v1.0.5)⁶¹ was employed to estimate the cellular proportion of different Mo-TAM clusters in each sample using bulk RNA-seq data from the Ivy GBM Atlas Project and TCGA database. Our human glioma scRNA-seq dataset with annotated Mo-TAM signature was used as a single-cell reference matrix. We computed the average expression matrices for each Mo-TAM cluster using the AverageExpression function in Seurat. The single-cell reference matrix, average expression matrices, and bulk RNA-seq data were utilized as inputs, while the other parameters were set as the algorithm's default options.

GSEA

GSEA was performed on the TCGA-GBM bulk RNA-seq dataset using the limma package to identify the molecular signatures associated with *ADM* expression. The corresponding gmt file for the indicated geneset was from the GSEA MSigDB. The samples were stratified into two groups according to the median level of *ADM*. Genes were sorted in descending order based on their Log2 fold change between *ADM*-high group and *ADM*-low group to create a genelist. The genelist was then subjected to enrichment analysis and visualized using the clusterProfiler package.

Bulk RNA-seq analysis of PBMC-derived M_φ

Total RNA was extracted from the human PBMC-derived M_φ exposed to TCM alone, or 1% O₂ alone, or both using RNAliso reagent (Takara Biotechnology). The RNA library was constructed and subsequent RNA sequencing was performed on the DNBSEQ platform (BGI-Shenzhen). FASTQ was used to check the read quality of the raw sequencing reads, and clean reads were aligned to the human reference genome (hg38) using the STAR aligner (v.2.7.1).⁶² Raw counts of protein-coding genes were obtained via featureCounts (v.2.0.3).⁶³ The aligned read counts by gene were converted into a count matrix, which was analyzed using DESeq2 (v.1.40.2)⁶⁴ package for counts normalization. Genes with log2 fold change ≥ 1 and adjusted $p < 0.05$ were considered as DEGs, which were converted to Entrez gene ID. The enrichKEGG function from the clusterProfiler package (v.4.8.1)⁶⁵ was employed for enrichment analysis. The dotplot function from the clusterProfiler package was utilized to visualize the enrichment results. For PCA analysis, we leveraged the fviz_pca_ind function of FactoMineR (v.2.8) to perform PCA dimensionality reduction on the normalized matrix. Data were visualized using R package ggplot2 (v.3.4.2).⁶⁶ To score the Hypoxia-TAM signature in differentially-polarized bulk M_φ, we extracted Hypoxia-TAM cluster signature genes derived from scRNA-seq and calculated the average expression of the Hypoxia-TAM signature genes in each bulk RNA-seq sample. Data were visualized using the R package ggplot2 (v.3.4.2).

Spatial transcriptomic analysis

Data preprocessing and normalization

The 10x Genomics Visium spatial transcriptomic data of hGBMs were derived from public datasets^{20,21,35} listed in the Key Resources Table. Sequencing reads were aligned to the human transcriptome reference GRCh38-2020-A using 10x Genomics SpaceRanger (v.1.3.0) and mRNA count matrices for each sample were produced. mRNA capture spot positions in the Visium slide were aligned with paired histology images using 10x Genomics SpaceRanger. We further integrated and processed SpaceRanger outputs using the Seurat package. Following the Seurat pipeline, we filtered out Visium spots with the number of counts $< 2,000$ and $> 35,000$, the number of genes < 500 , and a mitochondrion gene percentage $> 20\%$. Data normalization, scaling, and regression were conducted using the SCTransform method with vars.to.regress $<- c("percent.mt", "S.Score,"$ and "G2M.Score"). Two cases with poor image quality (GBM5_1 and GBM5_2 from GSE194329) were excluded from histology evaluation. After quality check and data filtering, we included 35 cases of hGBM spatial transcriptomic data for further analysis.

Spatial mapping of Mo-TAM clusters

To map different states of hGBM cells and Mo-TAM clusters to spatial transcriptomic data, we integrated hGBM scRNA-seq data with the 10x Genomics Visium mRNA count matrices using Cell2location (v.0.9.0).⁶⁷ Briefly, we leveraged a negative binomial regression model implemented in Cell2location and estimated the reference signature of different Mo-TAM clusters annotated in our scRNA-seq dataset. Donor IDs were regarded as the batch category and the following parameters were used to train the model: 'max_epochs' = 120, 'batch_size' = 2500, 'train_size' = 1. Myeloid-specific alterations calculated using the FindAllMarker function in Seurat were kept for deconvolution analysis of Mo-TAM clusters. Subsequently, we employed the reference signature model to decompose mRNA counts in spatial transcriptomic data and estimated the proportion of each Mo-TAM cluster in each spot. In this step, the following parameters in Cell2location were used: 'training iterations' = 100,000; 'number of cells per location N' = 20; 'detection_alpha' = 20.

Histology-transcriptome assignment

We plotted the Mo-TAM clusters in each slide and inferred the composition of Mo-TAM clusters in four distinct hGBM histological regions termed "Cellular tumor," "Infiltrating tumor," "Peri-necrotic region," and "Peri-vascular region" following the Ivy hGBM histological classification system.⁶⁸ These histological features of hGBM were manually evaluated by two experienced neuropathologists in our institute and assigned to each spot on the H&E images using Qupath (v.0.4.3).⁶⁹ The annotations were exported as GeoJSON files and mapped onto spatial transcriptomic spots for integrated analysis. The mean score of the Cell2location-computed cell proportion of each Mo-TAM cluster was calculated for each of these four histological regions separately. The results of the histology-transcriptome assignments were visualized using ComplexHeatmap (v.2.16.0).⁷⁰

Mapping hypoxia gradient and hypoxic niche features

We employed a case-by-case analysis strategy to map the hypoxia gradient and cellular features associated with the hypoxia gradient using hGBM spatial transcriptomic data. PCA dimensionality reduction was conducted on spatial transcriptomic spots using the RunPCA function in Seurat. The top 20 principal components were selected, and unsupervised clustering of spots was performed using the FindNeighbors and FindCluster functions in Seurat. The FindCluster function was set at a resolution of 0.8 as the optimal resolution. For each slide, the hypoxia score of each spot on the slide was calculated based on the expression of genes derived from a hypoxia geneset (HARRIS_HYPOXIA, MSigDB) using the AddModuleScore function in Seurat and assigned to the clusters generated by unsupervised clustering. Consecutive spots with an area > 2 mm² and an average hypoxia score > 0.4 were defined as hypoxia regions. The hypoxia neighborhood zone was defined as an area surrounding the hypoxia regions, where the hypoxia region boundary was extended outward by 1 mm in diameter. The SpatialDimPlot function in Seurat was used to visualize the hypoxia regions and hypoxia neighborhood zones embedding on the H&E staining image. The hypoxia gradient of hGBM tissues was generated by grading each spot in the hypoxia regions and neighborhoods into five hypoxia levels (ranging from level 0 to level 4) according to the hypoxia score of each spot. The cellular feature score was estimated using the AddModuleScore function in Seurat based on the averaged expression of the indicated genesets from the MSigDB. The mean score of the Cell2location-computed cell proportion or cellular feature was plotted separately for hypoxia regions and neighborhoods with different hypoxia levels.

Quantitative proteomics analysis

The quantitative proteomics analysis was performed using Metabo-Profile. A 36 h-cultured TCM and control medium alone were collected and centrifuged at 15,000 × g for 10 min at 4 °C, and the supernatants were quantified using the Bradford assay. Peptides were prepared using Pierce™ Quantitative Colorimetric Peptide Assay kit (Thermo Fisher Scientific) and labeled with Tandem Mass Tags 10-plex reagents according to the manufacturer's protocol (Thermo Fisher Scientific). Subsequently, the labeled peptides were fractionated using high-pH reverse-phase liquid chromatography and separated using an Agilent 300 Extend C18 column (Agilent). The proteome analysis was performed on an EASY 1200 nanoflow liquid chromatography (EASY-nLC™ 1200) instrument coupled to a Q Exactive™ HF-X mass spectrometer (Thermo Fisher Scientific). Raw mass spectrometry data were processed using Maxquant (v.1.6.15.0, Thermo Fisher Scientific)⁷¹ against the human Uniprot database,⁷² with a false-discovery rater < 0.01 at the level of proteins and peptides.

Metabolomics analysis

Metabolomics analysis was performed using Metabo-Profile. A 24 h-cultured Mφ-hypoxia-CM and Mφ-CM were collected and metabolites were extracted as previously described.⁷³ Metabolites associated with glycolysis were detected using ultraperformance liquid chromatography coupled to a tandem mass spectrometry (UPLC-MS/MS) system (Acquity UPLC I-Class/Xevo TQ-S, Waters). Chromatographic separations were performed on an ACQUITY BEH C18 column (Waters). The stability and repeatability of the instrument analysis were monitored using quality control samples. The raw metabolite data files generated using UPLC-MS/MS were processed using the MassLynx software (v.4.1, Waters) to perform peak integration, calibration, and quantitation for each metabolite.

Measurement of SPARC, lactate, and ADM production

For measuring the secreted form of SPARC, we cultured 1×10^6 hGBM-3 under normoxia (21% O₂) and PBMC-derived Mφ under normoxia or hypoxia (1% O₂) for 48 h. Subsequently, the conditioned medium from the abovementioned cells and the control medium without cell culture were collected, and SPARC production was detected using a human SPARC Quantikine ELISA kit (R&D Systems) following the manufacturer's instruction. For measuring secreted lactate, a 24 h-cultured conditioned medium from the abovementioned cells and the control medium were harvested, and lactate production was assessed using an L-lactate assay kit (Abcam). For measuring the secreted form of ADM, we treated 1×10^6 PBMC-derived Mφ with rhSPARC (10 µg/ml, R&D Systems), L-lactate (10 µM, Merck), or both for 48 h. The conditioned medium was then collected, and the ADM level was detected using an ELISA kit for human ADM (Phoenix Pharmaceuticals) according to the manufacturer's protocol.

TCM and hypoxia-TAM-CM

hGBM-3 or -4 (5×10^5 cells/well) or Hypoxia-TAM derived from PBMC or U937 (5×10^5 cells/well) were cultured in 2 ml serum-free medium in 6-well plates for 48 h. CM was collected, filtered using a 0.22 µm filter (Corning), and used immediately after collection.

Cell stimulation for p50 nuclear translocation

To determine whether p50 responses to TCM or hypoxia, PBMC-derived Mφ (2×10^4 cells /well in a 96-well plate) was cultured with TCM derived from 48 h-cultured hGBM-3, or under 1% O₂, or both for 1 h. To determine whether p50 responds to rhSPARC or lactate, PBMC-derived Mφ was treated with rhSPARC (10 µg/ml), L-lactate (10 µM), or both for 1 h. To determine whether blocking SPARC or inhibiting lactate formation impairs p50 activation, PBMC-derived Mφ was pretreated with TAK-242 (2.5 µM), or SO (10 mM), or both for 1 h, followed by the addition of hGBM-3-derived TCM and 1% O₂ for 1 h. The abovementioned cells were fixed for immunofluorescence staining of p50.

Immunofluorescence staining

Immunofluorescence staining was performed as previously described.^{17,74} Tissue sections of hGBMs or mGBM xenografts and slides of cultured cells were fixed in 4% paraformaldehyde for 15 min, blocked with 1% donkey serum and 0.3% Triton X-100 (Solarbio) for 30 min at 37 °C, and incubated with primary antibodies overnight at 4°C. The primary antibodies used are listed in the [key resources table](#). Unless otherwise indicated, sections were incubated with secondary antibodies labeled with Alexa Fluor 488, 555, or 647 (1:200; Thermo Fisher Scientific) and 4',6-diamidino-2-phenylindole (DAPI, Beyotime) and mounted using Fluoromount G (Southern Biotech). TUNEL (Beyotime) staining was performed according to the manufacturer's instructions. Confocal images were acquired using a Zeiss LSM900 microscope at 20× or 40× objective magnification. Multiplex immunostaining for ADM, CD31, and galectin-3 was performed using Opal Polaris 7 Color Automation IHC Detection Kit (AKOYA) and imaged using TissueFAXS Spectra Systems (TissueGnostics GmbH) at 20× objective magnification.

Immunohistochemistry staining

Immunohistochemistry staining was performed using the Dako REAL EnVision System according to the manufacturer's guidelines (Agilent). Primary antibodies include anti-p-ERK (Cell Signaling Technology) and anti-BRAF^{V600E} (Merck).

Intravital imaging of mGBM xenograft vasculature

Cranial imaging window surgery and intravenous injection of 70 kDa dextran-tetramethylrhodamine (Thermo Fisher Scientific) were performed on tumor-bearing mice for longitudinal intravital imaging of GL261 xenograft vasculature. Intravital images were captured using a Zeiss 780 multiphoton microscope with a complete z-stack of the tumor acquired at a depth of 200 μm and a step size of 4 μm. Simultaneous imaging of GL261 expressing cyan fluorescent protein (400–490 nm emission) and tumor vessels labeled with dextran-tetramethylrhodamine (560–680 nm emission) was performed using multiphoton excitation microscopy with excitation wavelengths of 840 and 960 nm.

In vivo vascular leakage, tumor hypoxia, and doxorubicin penetration

Alexa Fluor 647 cadaverine (1 kDa, 12.5 mg/kg, Thermo Fisher Scientific), pimonidazole hydrochloride (30 mg/kg, Hypoxyprobe), and doxorubicin (30 mg/kg, Merck) were administered via tail vein injection to tumor-bearing mice. Vascular leakage was quantified as the proportion of cadaverine⁺ areas in frozen sections of xenografts and adjacent normal mouse brain tissues. Pimonidazole adducts in frozen tumor sections were visualized using an allophycocyanin-labeled Hypoxyprobe antibody (Hypoxyprobe). Doxorubicin penetration was measured by determining the autofluorescence induced by doxorubicin (488–570 nm emission). The proportion of areas with doxorubicin effusion was quantified. All images were acquired using a Zeiss LSM900 confocal microscope at 20× or 40× objective magnification. The proportion of signal-positive area was defined as the ratio of the signal-positive field relative to the whole tissue field in at least five random fields per section and three sections per group using ImageJ (National Institutes of Health).

In vitro vascular permeability imaging assay

Endothelial adherens junction and intracellular permeability were analyzed using the *in vitro* vascular permeability imaging assay kit (Merck) according to the manufacturer's instructions. Biotinylated gelatin matrices were coated onto cell imaging dishes (Eppendorf). HBMECs were plated in 24-well plates at 25,000 cells/well and cultured for 48 h to achieve a confluent monolayer with well-developed cell-cell contacts. Subsequently, HBMECs were starved with serum-free medium for 16 h and treated with Hypoxia-TAM-CM or rhADM for 30 min. After that, cells were treated with fluorescein-streptavidin solution for 5 min, fixed with 4% paraformaldehyde for 30 min, and stained with anti-VE-cadherin and DAPI. Cells were imaged on a Zeiss LSM900 microscope.

Cell proliferation analysis

hGBM-3 cells were plated in 96-well plates at 500 cells/well, and cell viability was detected using a CCK-8 kit (Beyotime) on day 6.

TEM

TEM of vascular structure in hGBM xenografts and matched normal mouse brain tissues was performed as previously described.⁷⁵ Mice were anesthetized and perfused with PBS and subsequently with TEM buffer (4% paraformaldehyde and 2.5% glutaraldehyde in 0.1 M cacodylate buffer). The brain tissue was fixed in TEM buffer overnight at 4°C. Samples were embedded in Eponate 12 medium supplemented with DMP-30 (Ted Pella). Sections with a thickness of 80 nm were stained with uranyl acetate and lead citrate, and images were captured using an HT7700 electron microscope (Hitachi). TEM was performed on sections of at least five specimens/group. At least 10 tumor vessels and 10 normal vessels in each specimen were used for quantification.

MRI imaging

MRI imaging was performed using a 7T Pharmascan (Bruker BioSpin) equipped with a mouse head transmitter/receiver coil. Scanning sequences were as follows: T1-weighted imaging (FLASH, TE/TR: 1.82 ms/36.46 ms, field of view: 35 × 35 mm, matrix: 128 × 128, 6 flip angles: 5°, 10°, 15°, 20°, 25°, and 30°, slice thickness: 0.5 mm), DCE-MRI imaging (same geometry as T1-weighted images, TE/TR: 1.82 ms/36.46 ms, flip angle: 15°) with gadoteric acid (Gd-DOTA) administrated intravenously (0.1 mM/kg of body weight), contrast enhanced T1-weighted imaging (Turbo-RARE, TE/TR: 6.5 ms/987.03 ms, field of view: 35 × 35 mm, slice thickness: 0.5 mm). DCE-MRI images were processed on an Omni-Kinetics workstation (v.2.0, GE Healthcare), and the Patlak model was

employed for the quantification of Vp on DCE-MRI measured in mGBM xenograft areas. Regions of interest in each mGBM xenograft were manually drawn by the delineating xenograft border on the corresponding parametric images showing the maximum cross-sectional xenograft area on post-contrast T1-weighted images.

HPLC analysis

The AMA-pretreated or control mice bearing hGBM-4 xenografts were administered dabrafenib (30 mg/kg) dissolved in solution buffer (2% dimethyl sulfoxide, 45% polyethylene glycol 300, 2% Tween 80, and 51% double-distilled H₂O) by gavage. At pre-dosing (0 h) and 0.25, 0.5, 1, 3, and 6 h post-dosing, blood plasma and xenograft tissues were collected and analyzed using a SCIEX Triple Quad 5500+ LC-MS/MS System. Dabrafenib in plasma or xenografts was identified by matching the retention time peaks for the reference agent, and its levels were determined by measuring the area under the curve and maximum concentration.

Immunoblot analysis

Cells were lysed using radioimmunoprecipitation assay lysis and extraction buffer (Thermo Fisher Scientific). Total cells or cytoplasmic lysates were collected for immunoblot analysis as previously described.⁴ Primary antibodies are listed in the [key resources table](#).

Chromatin immunoprecipitation (ChIP)

The SimpleChIP Plus Enzymatic Chromatin IP Kit (Cell Signaling Technology) was used for ChIP assay according to the manufacturer's instructions. Cells were crosslinked with 1% paraformaldehyde and sonicated at 4°C for 5 min (3 mm probe with 30% power; Shengxi Ultrasonic Instrument). Chromatin was immunoprecipitated at 4°C for 3 h using 10 µl p50 antibody or isotype IgG (Cell Signaling Technology). Antibody–chromatin complexes were pulled down using ChIP-Grade Protein G Magnetic Beads, washed, and eluted using ChIP elution buffer. After crosslink reversal by treatment with 5 M NaCl and proteinase K (Cell Signaling Technology), immunoprecipitated DNA was purified and quantified using quantitative PCR.

Vector construction and production

Lentiviral vectors expressing shRNAs against *ADM* and *CRLR*, adenoviral vectors expressing shRNAs against *NKFB1*, *HIF1A*, and *JUN*, and shNT were constructed and produced by Shanghai Sunbio Bio-Medicine Technology with the shRNA sequences listed in [Table S6](#). Cells stably expressing shADM or shCRLR were enriched using puromycin selection. The *ADM* promoter region (2,000 base pairs ahead of the transcription start site) containing wildtype p50-binding sites or mutant p50 binding sites was cloned into AdMAX luciferase plasmid and packaged as an adenovirus (Shanghai Sunbio Bio-Medicine Technology).

Luciferase reporter assay

U937-derived Hypoxia-TAMs were transfected with luciferase vectors containing binding sites of p50 in the *ADM* promoter region, and cells were lysed 48 h post-transfection. A Dual-Luciferase Reporter Assay System (Promega) was used to measure the Renilla and Firefly luminescence signals, with the value of Renilla luminescence used for normalization.

Quantitative real-time PCR (qRT-PCR)

qRT-PCR was performed on a CFX96 Real-Time PCR Detection System (Bio-Rad). The primer sequences are listed in [Table S7](#).

QUANTIFICATION AND STATISTICAL ANALYSIS

Analysis summary

Detailed statistical analyses and software used are provided in the following subsections. All *p*-values < 0.05 were considered significant (**p* < 0.05; ***p* < 0.01).

Image processing

ImageJ, ZEN (v.3.6, ZEISS), and QuPath (v.0.4.3) were used for the quantification of confocal images. Multispectral imaging was pre-processed and quantified using StrataQuest software (v.7.1.119, TissueGnostics GmbH). The percentage of vascular area was calculated using AngioTool 0.5 (National Institutes of Health). The vascular skeleton was extracted using Avizo (v.2019.1, Thermo Fisher Scientific) to calculate join point density. The three-dimensional reconstructed images were fitted to vessels in the tumor area by the surface module in Imaris (v.9.0.1, Bitplane AG). For all images, the percentage of positive cells was defined as the ratio of positive cells versus total cells in each field. CD31⁺ tumor vessels and VE-cadherin signal in and outside the vascular segments were quantified using the pixel classification function in QuPath. VE-cadherin⁺ vessels were defined as the vessels marked by CD31 or laminin with colocalized VE-cadherin signal. The proportion of ADM⁺, CD31⁺, and galectin-3⁺ cells in hGBMs with necrosis feature was quantified in each 300-µm region from necrotic cores. Stained tissue specimens were quantified in at least five random 40× objective fields per section and three sections per group. Stained cultured cells were analyzed in at least 100 random cells for each group.

Statistics

Data were analyzed using GraphPad Prism 9, R software (v.3.6.3), and Python (v.3.7.4). No statistical methods were used to pre-determine the sample size. The investigators were not blinded to the allocation during the experiments or outcome assessments. The Kolmogorov–Smirnov test was used to assess the normal distribution of data. Two-tailed unpaired *t*-test, ANOVA, and two-sided unpaired Wilcoxon test were used for continuous variables. Survival analyses were performed using the Cox regression model or the Kaplan–Meier method with the Log-rank test for comparison. For boxplots, the centerline shows the median; box limits indicate the upper and lower quartiles; whiskers extend 1.5 times the interquartile range. Bar graphs are presented as mean ± SD or mean ± SEM as indicated in the figure legends. Unless otherwise noted, each experiment was repeated at least thrice using biologically independent samples.